Exploring the Chemistry of Re^I: Physical and Theoretical Investigations

by

Philip D. Bulsink

Thesis submitted to the
Faculty of Graduate and Postdoctoral Studies
In partial fulfilment of the requirements
For the degree of

Master of Science
In
Chemistry

Ottawa-Carleton Chemistry Institute
University of Ottawa

Supervisors: *Professors Darrin Richeson & Tom Woo*

Abstract

The development of Rhenium I photocatalysts has been pursued since Lehn first showed the excellent performance of the Re^I bipyridine tricarbonyl catalyst. Since then, development has modified the organic ligand to demonstrate continued or improved activity with other α-diimine bidentate geometries. Geometry has been limited to κ_2 motifs, with fac-$(CO)_3$ and axial halide. This work will demonstrate the synthesis, characterization, and testing of a new $\kappa_3(L_3)$-Re^1-mer-$(CO)_2$X (X = Cl, Br, CN, OTf) family of compounds for CO_2 reduction, as well as computational investigations into the mechanism of the reduction,

Acknowledgements

Thanks to the members of the Richeson and Woo research groups, both past and present, for the assistance provided and for making the time spent researching and writing this thesis enjoyable. Thanks as well to Frank and Sean in the Brusso lab, for their willingness to allow use of their characterization equipment. Thanks to Jake and the Gambarotta laboratory for use of their GC, and to the Sciano Lab, especially Janice, Charles, and Deni, for the use of their photolysis equipment.

I'd like to thank Dr. Ilia Korobkov for his work measuring and solving the x-ray crystal structures of the compounds discussed. He assisted with some paper writing as well.

Finally, I'd like to thank my fianceé Leanne, and my parents for their unending support, and understanding when I came home frustrated or exhausted from work.

Contents

List of Tables

List of Figures

Chapter 1

Introduction

1.1 Inorganic Chemistry

Common distinctions split most chemical compounds into one of two categories: organic and inorganic. Organic molecules contain carbon and hydrogen, with or without additional nitrogen, oxygen, phosphorus, sulfur, and the halides. Inorganic chemistry is, therefore, considered to be the remainder of the molecules possible. While they may include come aspect of organic chemistry (especially in organometallic molecules), the main structural motif or reactive center is a non-organic feature. These inorganic compounds can range from compounds such as lithium or grignard reagents with significant organic influence, to metallic alloys or mineral compounds. With such a wide range of possibilities, inorganic chemistry has many facets. A widely active research area is the development and testing of transition metal complexes for catalytic, photo-physical, biochemical or manufacturing uses.

1.2   Photochemistry & Catalysis

A report of the first synthesized organometallic complex was published by Zeise in 1831.[1] To form what is now known as Zeise's salt, $K[PtCl_3(C_2H_4)] \cdot H_2O$, he mixed platinum chloride with ethanol, followed by a reaction with potassium chloride.[2] After some controversy to the composition of this, it was confirmed by Griess and Martius,[3] and later expanded upon by Birnbaum.[4]

The field of organometallics was expanded greatly by Frankland,[2] and many of his complexes were catalytically active. Further development of this new type of chemistry quickly led to useful catalysts for the conversion of petroleum products or the production or destruction of other chemicals to be developed using nearly all of the transition metals. These catalysts take all forms, from simple olefin and halide compounds to multi-metallic complexes with large organic ligands.

Some of the most significant organometallic catalysts since the late 1990s have been the development of earth metal pincer complexes to replace noble metal or early transition metal catalysts, which are often more toxic or expensive to produce. Brookhart and Gibson (at DuPont) published a series of papers[5–8] on the use of iron and cobalt with bis(imino)pyridine ligands to perform ethylene polymerization at rates exceeding those of similar noble metal complexes and metallocenes.[9] The role of the ligand in the mechanism is still up for debate, but many modified systems have been synthesized and tested since the first work was published.[10]

Many of these types of pincer complexes are photochemically active. In transition metal complexes, the interaction between the metal atom(s) and the ligands can cause significant electron mobility upon the absorption of incident photons. The metal atom's d orbitals typically lie at or near the Highest Occupied Molecular Orbital (HOMO) energy, while the ligands often have low energy anti-bonding orbitals (π^*) at the Lowest Unoc-

cupied Molecular Orbital (LUMO) levels. When a photon is absorbed and is promoted from the ground state to the excited state, that state is geographically removed from the metal centre, this motion of the electron is labelled a Metal-Ligand Charge Transfer (MLCT). Formally, the metal atom is oxidized by the photons, this oxidation allows for redox reactivity at the metal centre for as long as the electron remains removed to the ligand. Relaxation (through photon emission via fluorescence or phosphorescence, or via vibrational or other motion processes) can return the electron to the metal to reform the ground electronic state.

1.3   Rhenium

Rhenium compounds in particular are known to have a broad range of applications in coordinated environments. Their use in catalysis has been explored, covering olefin hydrogenation,[11] epoxidation (with chiral selectivity),[12] and in a host of organic bond formation reactions[13] (Friedel-Crafts acylation and alkylation,[kuninobu2009, 14,15] nucleophilic addition,[16,17] carbon-carbon coupling,[18,19] as well as other heteroatom-carbon bond formation[20–24]). Rhenium has also been used in radiopharmaceutical applications, due to the availability of moderately radioactive isotopes.[25,26] It exhibits other interesting fundamental photophysical properties as well.[27]

Since the mid-1970's, complexes containing the α-diimine Re$^{\mathrm{I}}$ tricarbonyl core have attracted a great deal of attention due to their attractive photochemical properties. The pseudo-octahedral *fac*-[L$_2$Re(CO)$_3$X] and *fac*-[L$_2$(L′)Re(CO)$_3$]$^+$ complexes have been the dominant species.[28–38] A large family of compounds with these formulations have been accessed by the addition of chelating diimine σ-donor ligands to [Re(CO)$_5$X] with the quantitative replacement of two *cis* carbonyls in the Re$^{\mathrm{I}}$ starting material.[28,39–46] Significantly, these reactions form only bidentate coordinated ligands with *facial* tricarbonyl isomers

as products even when a potentially tridentate σ-donor, such as bis(imino)pyridine or 2,2':6',2"-terpyridine. are employed in the reaction (Figure 1.1).[potgieter2013, 47–49]

These robust species have been examined for potential applications in organic light-emitting diodes (OLEDs),[50,51] chemosensors and biotechnology probes,[52–56] fluorescence microscopy imaging of cells,[52,57,58] and the photochemical reduction of CO_2 to CO.[59–63] Among the key photophysical features of these α-diimine Re^I compounds is the electron transfer capability of this system and the interplay between the Re center and the well-known non-innocent redox activity of the ligands.[lyaskovskyy2012, 64]

X = Cl, Br, I
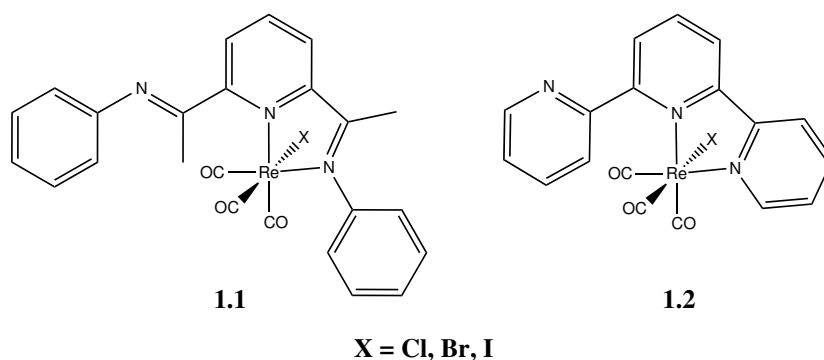
Figure 1.1 Two common fac-[$L_2Re(CO)_3X$] complexes with terdentate σ-donor ligands: L = bis(imino)pyridine (**1.1**) and 2,2':6',2"-terpyridine (**1.2**)

redraw figure for 1.1 and 1.2

Further development of this chemistry has been restricted by the limited structural and electronic variability of the common pseudo-octahedral fac-[$L_2ReX(CO)_3$] (L_2 = α-diimine) products. While these systems continue to receive considerable attention, studies detailing the coordination chemistry of the meridionally-coordinated tridentate triimine Re^I dicarbonyl core are quite limited.[65] For example, while κ^3(terpy)Re(CO)$_2$Cl was initially reported in 1988,[66] closer analysis of the reported analytical data (including ^{1}H NMR) indicate that this compound is more likely κ^2LRe(CO)$_3$Cl. A more recent report for this compound provides spectroscopic details of this species as well as the

preliminary report for the generation of $[\kappa^3(\text{terpy})\text{Re(CO)}_2\text{L}']^+$ cations (L = PPh_3, PEt_3, NC_5H_5, and NCCH_3).[67] Finally, the ^{1}H NMR data for $\kappa^3(\text{terpy})\text{Re(CO)}_2\text{Br}$ has been reported[49] but accompanied no other characterization.

In order to fully exploit the potential of this versatile family of compounds, the limits imposed by the bidentate coordination need to be addressed. Furthermore, it would appear that, on the basis of the tridentate ligands that have been investigated, the concerted effort to produce the tridentate species has been essentially unsuccessful, or requiring harsh conditions.**potgieter2013** Attracted by this challenge we sought to synthesize, crystallographically authenticate, and investigate the photophysical properties of low-valent rhenium pincer complexes displaying an N,N',N"-chelated terpyridine array.

Prior work in our lab recently reported the conversion of bidentate bis(imino)pyridine complexes 2,6-$\{2,6\text{-Me}_2\text{C}_6\text{H}_3\text{N=CPh}\}_2(\text{NC}_5\text{H}_3)\text{Re(CO)}_3\text{X}$ (X = Cl, Br) into tridentate pincer ligand compounds, 2,6-$\{2,6\text{-Me}_2\text{C}_6\text{H}_3\text{N=CPh}\}_2(\text{NC}_5\text{H}_3)\text{Re(CO)}_2\text{X}$ (X = Cl, Br).[65] This transformation was performed in the solid-state by controlled heating of these bidentate species above 200°C in a tube furnace under a flow of nitrogen gas giving excellent yields ($\geq$ 95%). These compounds defined a new coordination environment for Re^I carbonyl chemistry where the metal center is supported by a planar, tridentate pincer coordinated bis(imino)pyridine ligand.

Complexes of 2,2':6',2"-terpyridine (terpy) are of interest due to the conceptual relationship to established bis(imino)pyridine compounds.[68,69] This thesis will be a discussion of the development of chemistry of Re^I complexes, their characterization, and comparison of structural and photo-physical properties to computed values. Further exploration of the CO_2 reduction by photo-catalysis of these new complexes will be analyzed. This thesis will also take a more detailed look at specifics of the mechanisms proposed for current Re^I diimine catalysts, and propose new geometries for prior mechanistic steps

Take out spoilers

based on experimental, computational, and literature review work.

Chapter 2

New Coordination Geometries for Re$^{\text{I}}$

2.1   Introduction

As mentioned previously in the introduction, Re$^{\text{I}}$ compounds have been typically biden-
tate (κ^2) compounds, even when using a potentially terdentate (κ^3) ligand such as
bis(imino)pyridine or terpyridine (refer to Figure 1.1). The chemistry of this rhenium
α-imino complex has been extensively invesigated, with over 1700 references appearing in
a structure search for that metal-ligand motif. The extraction of an additional carbonyl
and the chelation of the pendant arm of the ligand was attempted to extend the pi sys-
tem of the ligand and its interaction with the metal centre. This was first demonstrated
by prior work in our group for the bis(imino)pyridine ligand.[65]

2.2 Synthesis of Bidentate and Terdentate Re^I Complexes

Similar to the prior work, synthesis began with the production of the bidentate complex κ^2(terpy)Re(CO)$_3$X (X = Cl, Br) by coordination of 2,2':6',2"-terpyridine (Sigma) with a Re(CO)$_5$X (Strem) starting material in dry toluene at reflux for 4 hours, as shown in Scheme 2.1. A bright yellow powder precipitated from solution and was collected by filtration, washed with cold hexanes, and dried *in vacuo* to a good yield of **2.1** and **2.3** respectively.[i] These bidentate compounds were characterized fully and used without further purification to produce κ^3(terpy)Re(CO)$_2$X (X = Cl, Br) via thermolysis, as well as for anion exchange reactions.
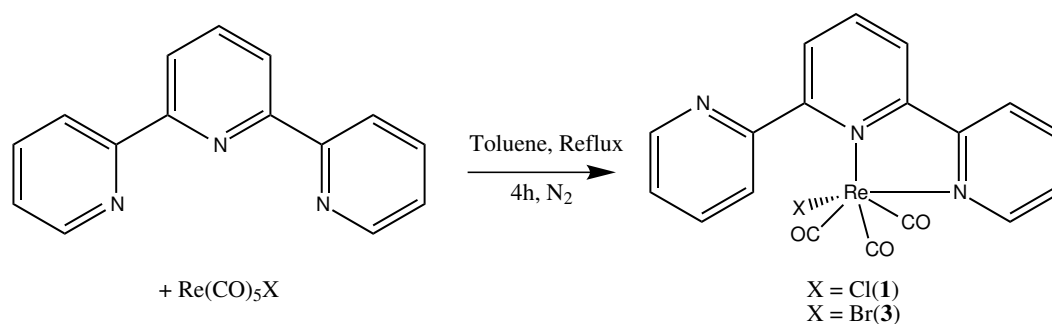
Scheme 2.1 Synthesis of **2.1** and **2.3** from Re(CO)$_5$X and 2,2':6',2"-terpyridine

Conversion of compounds **2.1** and **2.3** to the κ^3 moiety required the release of CO and the subsequent coordination of the free pendant arm. Prior work had identified the thermal lability of the carbonyl, based on a method first described by Buckingham with a osmium complexes.[70] In this method, a ceramic sample boat was placed in a tube furnace at elevated temperature, under a flowing atmosphere of N$_2$. After some time, the sample is removed and collected at nearly quantitative yield. Determination of

---

[i]Experimental details for all compounds can be seen in Appendix A Experimental Procedures

the appropriate thermolysis temperature was performed by Thermogravimetric Analysis (TGA) of the sample. A 6-8 % mass loss (dependant on sample) indicated the departure of one carbonyl group from the complex. Results of TGA on **2.1** and **2.3** is shown in

discuss extra Figure 2.1.

Thermogravimetric Analysis of k^{2}Re(CO)$_3$X
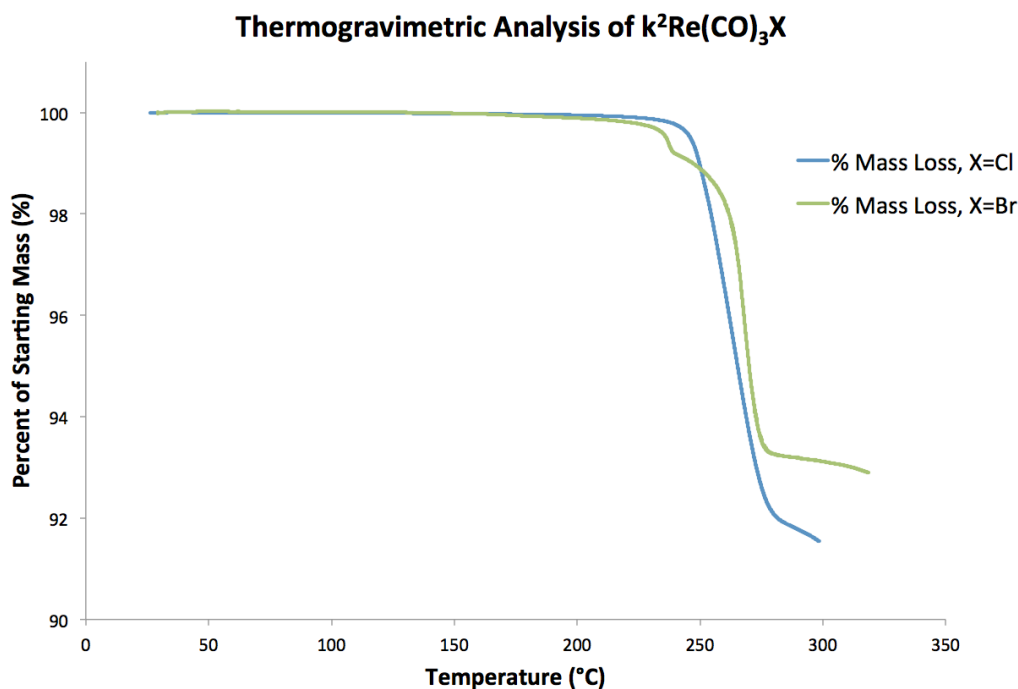
Figure 2.1 Results of TGA analysis on **2.1** and **2.3**

The onset of mass loss in the TGA of **2.1**, and the onset of the main mass loss in the TGA of **2.3** were chosen to identify a thermolysis temperature for each sample. For **2.1**,

check that value thermolysis was performed at 240°C, and for **2.3** thermolysis was performed at 260°C, yielding **2.2** and **2.4** respectively, at quantitative yields, by the pathway in Scheme 2.2.

Further reactions were carried out on the above products to yield triflate and cyano complexes in bidentate and terdentate geometries. These anion exchange reactions were performed by the addition of the silver salt to **2.1** or **2.2**, to precipitate AgCl, leaving κ^2(terpy)Re(CO)$_3$CN (**2.5**), κ^3(terpy)Re(CO)$_2$CN (**2.6**), κ^2(terpy)Re(CO)$_3$OTf (**2.7a**)
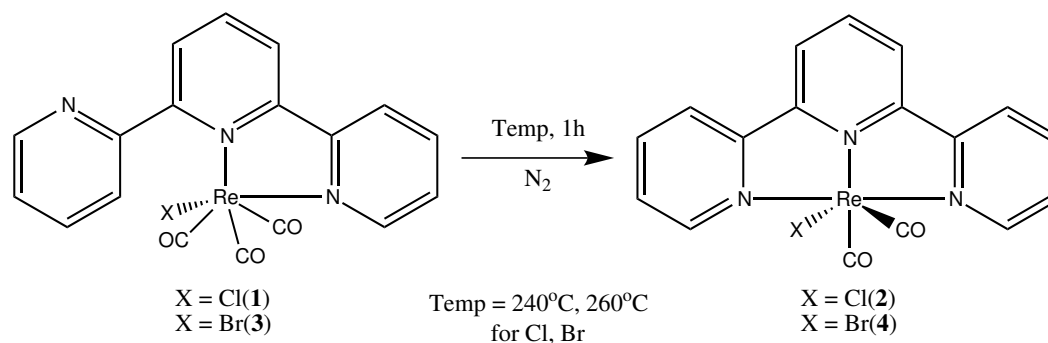
Scheme 2.2 Synthesis of **2.2** and **2.4** by thermolysis of **2.1** or **2.3**, respectively

and κ^3(terpy)Re(CO)$_2$OTf (**2.8a**), as shown in Scheme 2.3. Resulting in only moderate yields, **2.7b** and **2.8b** were synthesized by the direct addition of neat triflic acid (CF$_3$SO$_3$H) to **2.1** and **2.2** respectively. HCl was released, the solutions were quenched by addition of aqueous NaCO$_3$, and product was collected, again at moderate yield.
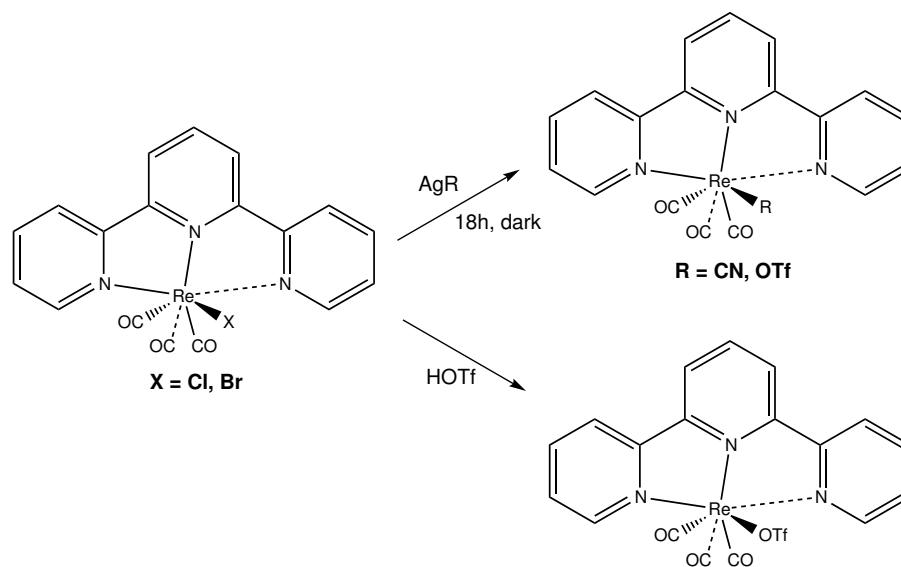
Scheme 2.3 Anion exchange pathways to synthesize **2.5** - **2.8**

2.3   Characterization

Characterization was performed on each of the products synthesized as discussed above. Nuclear Magnetic Resonance (NMR) analysis, x-ray crystallography, as well as UV-Vis and IR spectroscopy was performed. Computational Density Functional afd (DFT) methods were used to solve the geometries, and Time Dependant Density Functional Theorem (TD-DFT) was performed to predict UV-Vis spectra and identify electronic transitions.

2.3.1   NMR Analysis

Proton NMR was performed on each of the samples. Each sample was dissolved completely in deuterated acetonitrile (CD_3CN) and analysis was performed on a Bruker AVANCE 400 MHz spectrometer. Data was processed from the FID signal via the Top-Spin program, and spectra were analyzed using ACD NMR Processor v12.0.

Detailed peak analysis comparing bidentate samples **2.1**, **2.3**, **2.5**, and **2.7** (Figure 2.2) or terdentate **2.2**, **2.4**, **2.6**, and **2.8** (Figure 2.5) show little difference between samples. This is due to the distance between the anion and any protons on the ligand. While anions with different σ donor strength marginally impact the metal-ligand interactions, these have only small effect on the location of peaks, shifting between samples by typically less than 0.1 ppm. As is shown in **??**, the characteristic shape of each spectra remains constant, only exact peak locations and some peak order varies with anion choice.

check compounds & spectra

The characteristic feature in the NMR spectra after the transformation from bidentate to terdentate (e.g. sample **2.1** to **2.2**) is the simplification of the signals in the aromatic region (between 7 and 9 ppm). This simplification is due to the increased symmetrization
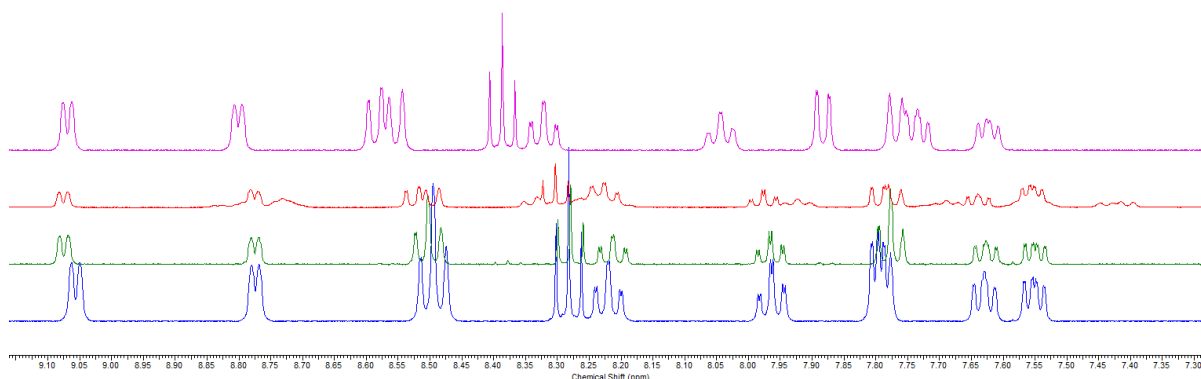
Figure 2.2 The aromatic region of the ^{1}H NMR spectra for compounds **2.1** (blue), **2.3** (green), **2.5** (red) and **2.7** (purple)

of the ligand, while the κ^2-bidentate ligand has a freely rotating pendant group, the κ^3-terdentate ligand is in a more rigidly fixed geometry. Prior work in literatureand in our group[71] shows the temperature dependence of the rate of rotation of this pendant arm for various ligand species.
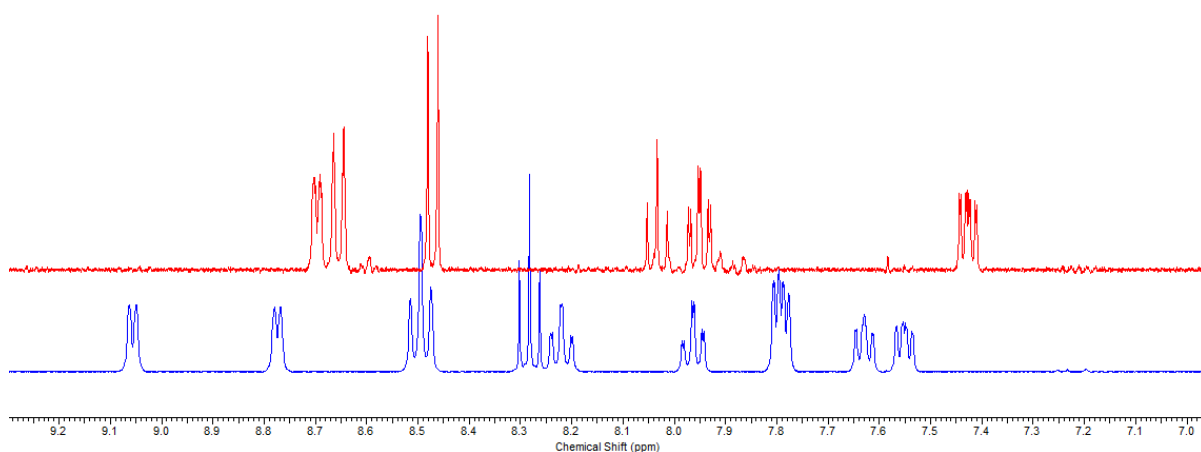
Figure 2.3 The aromatic region of the ^{1}H NMR spectra for compounds **2.1** (blue) and **2.2** (red), showing the simplification of the spectra upon the conversion from bidentate to terdentate

The simplification of peaks due to the symmetrization of the ligand results in the peaks from free pendant arm protons *a*, *b*, *c*, and *d* (see Figure 2.4) with peaks at 9.06, 7.63, 8.22 and 7.79 ppm, respectively, aligning with their mirroring peaks at *a'*, *b'*, *c'* and *d'* (with peaks at 8.77, 7.55, 7.96, and 7.80 ppm). The new symmetrized peaks show integrations of two protons per peak, verified by the single proton (*f*) peak from the central pyridyl ring, *para* to the nitrogen. As well, the presence in metal-ligand charge interaction in the pendant arms reduces the deshielding, shifting the free pyridyl *ortho* proton from 9.06 ppm to 8.77 in the chelated, with similar shifts evident for the other pendant protons .
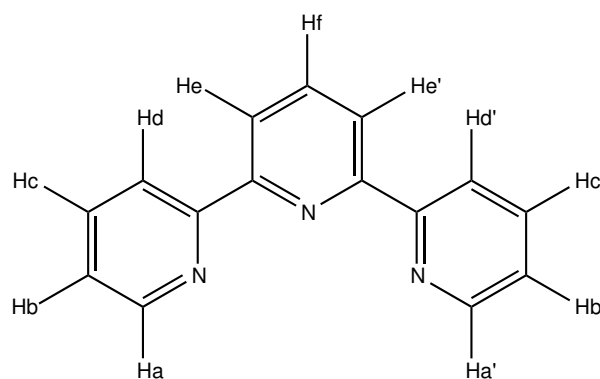
Figure 2.4 Proton-explicit skeletal drawing of 2,2':6',2"-terpyridine

As in the case of bidentate compounds, modification of the anion has only minor effects on the NMR spectra. This is the expected behaviour, the conjugated pi system and the lack of protons near the modified anion combine to be susceptible in only a minor fashion.

Carbon NMR (^{13}C) was attempted on the complexes as well. Unfortunately, Re^I complexes perform poorly in ^{13}C NMR experiments, the signal to noise ratio is incredibly poor (if a signal is even visible). The effect of this is a lack of ^{13}C NMR analysis of these
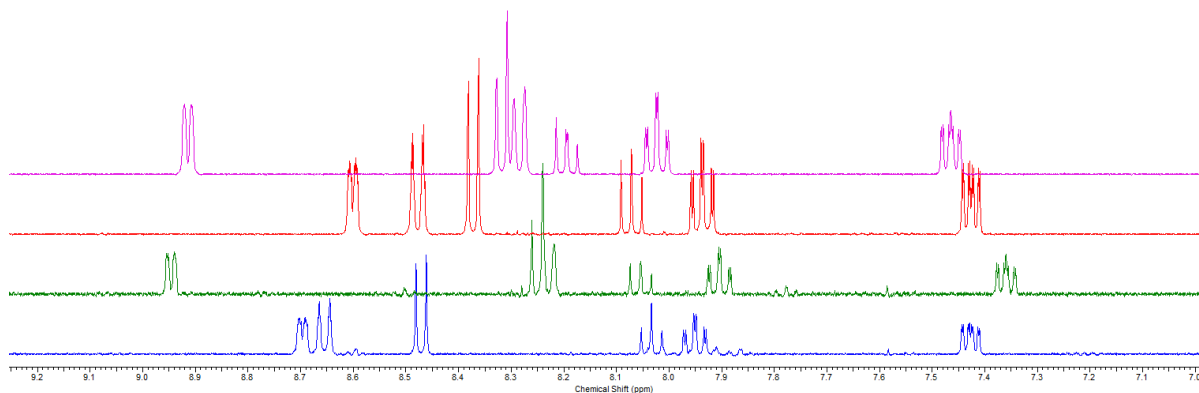
Figure 2.5 The aromatic region of the ^{1}H NMR spectra for compounds **2.2** (blue), **2.4** (green), **2.6** (red) and **2.8** (purple)

compounds in literature, with a very few exceptions. Extensive efforts included use of a 500 MHz spectrometer, with to produce the best example, seen in Figure 2.6, with average peak signal to noise ratio (s/n) of only 4 to 5.

Topspin shows scan numbers?
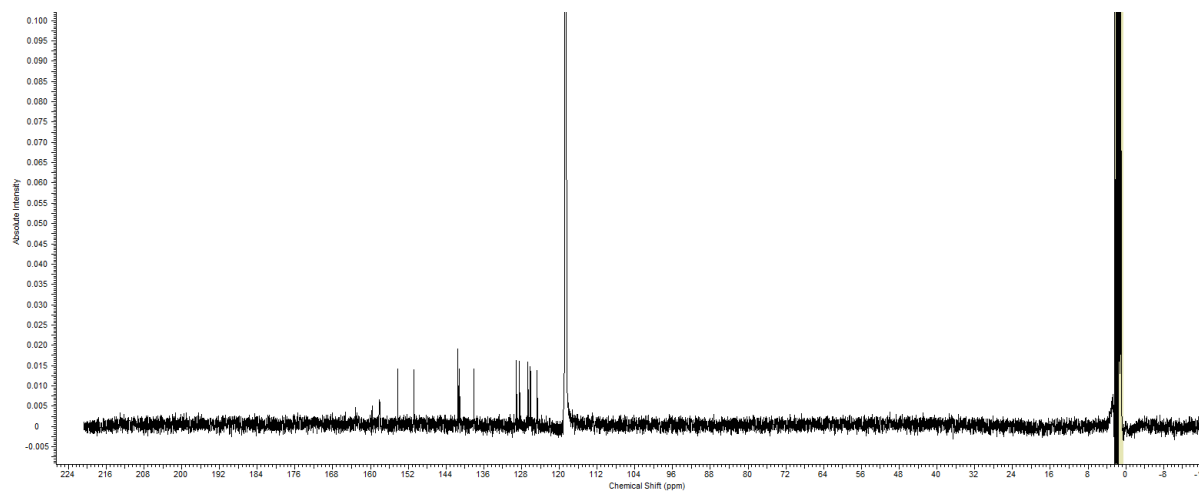
Figure 2.6 The ^{13}C NMR spectra of **2.1**. Spectra for other compounds could not be collected

2.3.2 Structure Analysis with X-Ray Crystallography and DFT

Single crystal analysis by x-ray crystallography yielded good structures of compounds **2.1**, **2.2**, **2.3**, **2.4**, . These are the first reported crystal structures of the κ^3 terdentate Re^I compounds. A number of structural characteristics are common between the various bidentate or terdentate complexes. Much analysis has been done on the structures of bidentate complexes in literature, the notable characteristic within terpyridine compounds is the rotation of the pendant arm pushing the nitrogen atom away from the plane of the metal-ligand bonds by approximately 100°. Cell parameters and other collection data for compounds **2.1**, **2.3**, **2.5**, and **2.7** are located in Table 2.1.

Table 2.1 Crystal data and structure refinement for compounds **1**, **3**, **5**, and **7**

Compound	1	3	5	7
Empirical formula	$C_{19}H_{11}N_3O_3ReCl$	$C_{19}H_{11}N_3O_3ReBr$	$C_{20}H_{11}N_4O_3Re$	$C_{22}H_{14}N_4O_6F_3SRe$
Formula weight (g/mol)	538.96	583.41	530.04	693.63
Temperature (K)	200(2)	200	200	200
Wavelength (Å)	0.71073	0.71073	0.71073	0.71073
Crystal System	Triclinic	Monoclinic	Triclinic	
Space Group	P-1	C2/c	P-1	
a (Å)	9.8736(4)	31.1537(7)	9.9196(9)	
b (Å)	14.8202(4)	7.1176(2)	14.9902(14)	
c (Å)	16.3472(4)	16.8519(4)	16.5187(15)	
α (deg)	69.2890(10)	90.000	68.363(2)	
β (deg)	80.801(2)	111.0230(10)	80.929(2)	
γ (deg)	79.836(2)	90.000	79.975(2)	
Volume (Å^3)	2190.00(12)	3488.00	2236.6(4)	
Z, r (calc) (Mg/m^3)	2, 1.997	8, 2.222	2, 1.927	
Absorption coefficient (mm^{-1})	6.063	9.282	5.821	
Absorption correction		Semi-empirical from equivalents		
Final R indices [I$\geq$2σ(I)]	R1 = 0.0397, wR2 = 0.0839	R1 = 0.0232, wR2 = 0.0614	R1 = 0.0390, wR2 = 0.0921	
R indices (all data)	R1 = 0.0604, wR2 = 0.0951	R1 = 0.0285, wR2 = 0.0642	R1 = 0.0500, wR2 = 0.0961	

In addition, the structures of all species were optimized using Gaussian 09[72] employing the B3LYP[73,74] exchange-correlation (XC) functional. The LanL2DZ basis set/effective core potential[75] was used on Re, and the all-electron TZVP basis set[76] for the remaining lighter atoms. Frequency analysis of all structures was used to confirm the nature of

the stationary points. Solvent effects were computed when necessary using the integral equation formalism variant of the Polarizable Continuum Model (PCM) for solvation within Gaussian 09.[77,78]The results of these calculations are compared to the x-ray crystallography data in the tables below.

> Compare xray to computational structures in tables and discussions

Sample **2.3**s crystal structure had a higher symmetry than the other samples. Details on the exact methods used for structure elucidation are available in section A.3, but all of the structures found are of high quality. The structures of **2.1**, **2.3**, and **2.5** can be seen in Figure 2.7. More views of these structures can be seen in Appendix section A.3. Crystals suitable for x-ray analysis were unable to be collected from compound **2.7**.

Selected bond lengths, bond angles, and torsions are listed in Table 2.3, Table 2.4 and Table 2.5 for products **2.1**, **2.3**, and **2.5** respectively. The structures can be seen in Figure 2.7a, Figure 2.7b and Figure 2.7c, and more views of these structures can be seen in Appendix A, subsection A.3.1, X-Ray Structures from Multiple Vantage Points.

The Re^I centre in the pseudooctahedral complex is supported by a planar, pincer coordinated ligand defined by the terminal and central pyridyl group of the terpyridine. One of the carbonyl groups lies in this plane trans to the central pyridyl group, while the remaining carbonyl groups and the anionic group or other complexed species lie on an approximately perpindicular plane to the ligand. Bond angles around the Re centre show a significant deviation of up to 15° from the ideal octahedral geometry for all samples analyzed. The typical N-Re-N bond angle of 75° is due to the atomic size of rhenium, comparison to the crystal structure of an analogous compound with a manganese atom[79] shows an increase in the bonding angle by approximately 4° due to a decrease of bond length from metal to nitrogen of about 0.12 Å for both the central and terminal pyridines.

The deviation from octahedral is further visible in the rotation of the X-Re-CO plane

(a) X-ray crystal structure for **2.1**

(b) X-ray crystal structure for **2.3**

(c) X-ray crystal structure for **2.5**
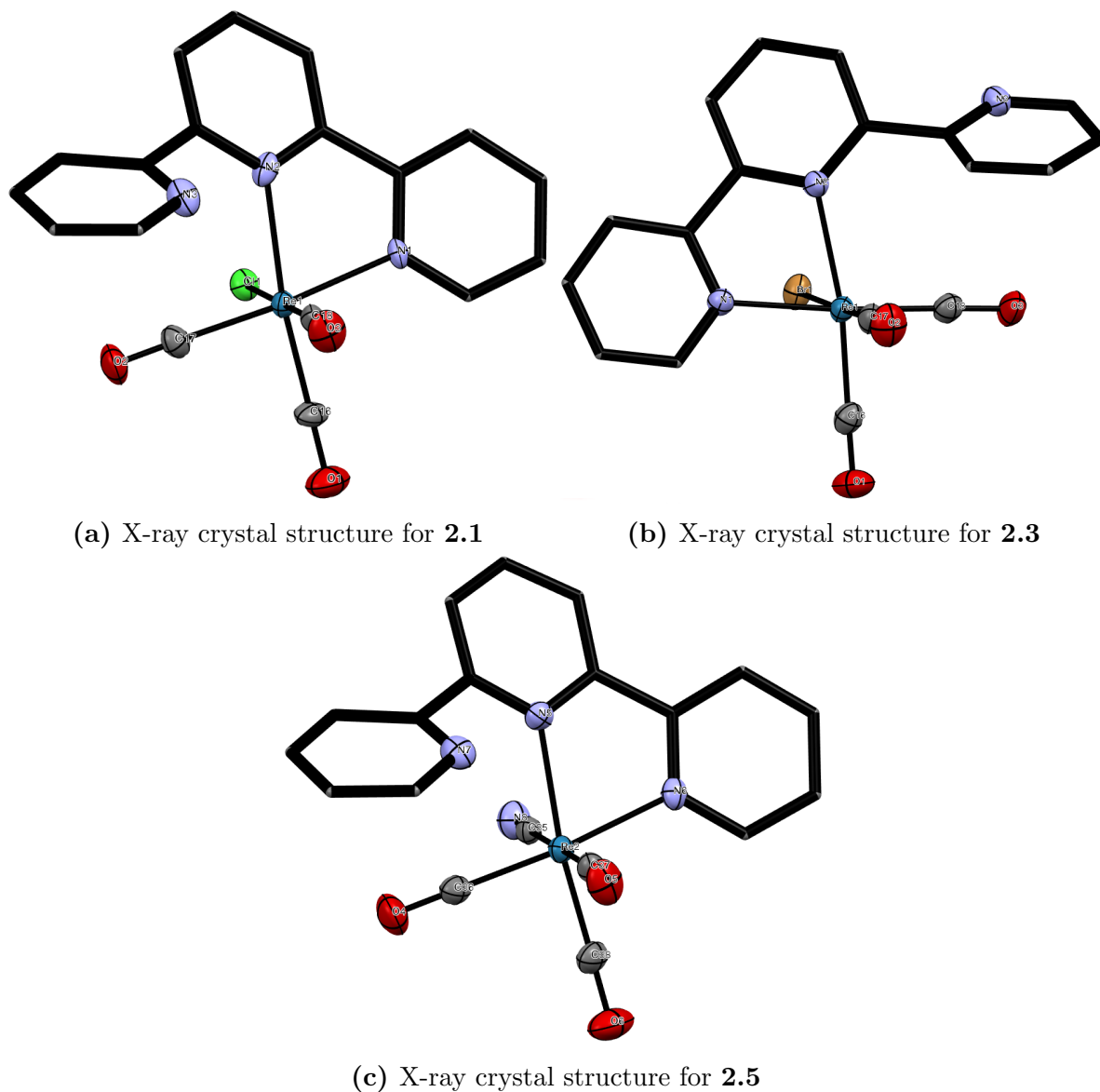
Figure 2.7 X-ray crystal structure representation for **2.1**, **2.3**, and **2.5**. Co-crystallized chloroform, hydrogen atoms, and thermal ellipsoids of ligand carbon atoms are omitted for clarity.

(X=halide, anion, complexed group) by approximately 10 degrees from the right angle relative to the plane of the ligand. The axial halide, anion, or chelated group typically occupies a position such that it is slightly eclipsing the ligand, when viewed from the axial position. This eclipsing is due to some unknown process, no steric interfer-

ence exists upon that site, analysis of electrostatic or other short-range electronic effects computationally show any interaction between this site and the aromatic rings. In Re^I complexes, the halide or anion is located axial relative to the plane of the ligand. For the acetonitrile complex with triflate counterion, the acetonitrile occupies the axial position. This site occupation holds through the complete set of x-ray crystal structures with a $\kappa^2-(\text{bipy})\text{Re(CO)}_3\text{X}$ core structure motif deposited in the Cambridge Crystallography Data Centre (CCDC) database,[80] and extends through other α-diimine complexes seen in our lab and in literature.[65]

The crystal structure for compound **2.5** contains two molecules per unit cell, one of which is solved to have the cyano group in the position trans to the ligand. However, careful analysis of the bond lengths, angles, and torsion data in Table 2.5 shows a remarked similarity between all -CO and -CN groups. Additionally, in an x-ray diffraction pattern, -CN and -CO look quite similar. Thus, while the structure solved to the two isomers, critical analysis would suggest that this molecule does not violate the axial position pattern laid out above. The computed structures energies in Table 2.2 show a favouring of the axial position by 12-16 kJ/mol in the gas phase and by PCM in a simulated acetonitrile solvent.

Table 2.2 Solvated and Gas Phase Energies of Axial & Trans $\kappa^{\text{x}}-(\text{terpy})-\text{Re(CO)}_{5\text{-x}}\text{CN}$ (x=2,3)

Geometry	Bidentate		Terdentate	
	E(gas)[a]	E(solution)[b]	E(gas)[a]	E(solution)[b]
Axial	-1254.96132	-1254.99059	-1141.57255	-1141.60827
Trans	-1254.93788	-1254.97168	-1141.54660	-1141.58209
Difference	0.02343	0.01891	0.02595	0.02612
Difference (kcal/mol)	14.70	11.87	16.28	16.43

[a] B3LYP SCF energy in hartrees.
[b] B3LYP SCF energy in hartrees with PCM solvation in acetonitrile.

Selected bond lengths, bond angles, and torsions are listed in Table 2.3, Table 2.4 and Table 2.5 for products **2.1**, **2.3**, and **2.5** respectively.

Table 2.3 Selected Distances, Angles, and Torsions for **1**

Bond	Distance (Å)	
	Experimental	Calculated
Re(1)-C(16)	1.89(1)	1.916
Re(1)-C(17)	1.934(8)	1.936
Re(1)-C(18)	1.90(1)	1.918
Re(1)-N(1)	2.162(6)	2.197
Re(1)-N(2)	2.236(9)	2.293
Re(1)-Cl(1)	2.496(2)	2.525

Angle	Degrees (°)	
	Experimental	Calculated
C(16)-Re(1)-C(17)	87.6(4)	86.877
C(16)-Re(1)-C(18)	88.3(4)	90.613
C(17)-Re(1)-C(18)	87.3(4)	89.557
C(16)-Re(1)-N(1)	96.4(3)	96.240
C(17)-Re(1)-N(1)	174.9(3)	175.600
C(18)-Re(1)-N(1)	95.9(3)	93.506
C(16)-Re(1)-N(2)	169.3(3)	170.368
C(17)-Re(1)-N(2)	101.1(3)	102.755
C(18)-Re(1)-N(2)	98.3(3)	89.415
N(2)-Re(1)-N(1)	74.5(3)	74.146
C(16)-Re(1)-Cl(1)	91.7(3)	91.453
C(17)-Re(1)-Cl(1)	91.7(3)	94.786
C(18)-Re(1)-Cl(1)	179.9(3)	175.286
N(1)-Re(1)-Cl(1)	84.0(2)	82.058
N(2)-Re(1)-Cl(1)	81.6(2)	87.840
O(1)-C(16)-Re(1)	179.6(9)	178.224
O(2)-C(17)-Re(1)	176.0(8)	176.907
O(3)-C(18)-Re(1)	177.3(9)	179.317

Torsion	Degrees (°)	
	Experimental	Calculated
N(1)-C(5)-C(6)-N(2)	16(1)	15
N(2)-C(10)-C(11)-N(3)	41(1)	139

Table 2.4 Selected Distances, Angles, and Torsions for **3**

Bond	Distance (Å)	
	Experimental	Calculated
Re(1)-C(16)	1.911(3)	1.91740
Re(1)-C(17)	1.890(3)	1.91814
Re(1)-C(18)	1.921(4)	1.93897
Re(1)-N(1)	2.173(3)	2.19687
Re(1)-N(2)	2.232(2)	2.28998
Re(1)-Br(1)	2.6410(4)	2.67953
Angle	**Degrees (°)**	
	Experimental	Calculated
C(16)-Re(1)-C(17)	89.1(1)	90.772
C(16)-Re(1)-C(18)	85.9(1)	86.823
C(16)-Re(1)-N(1)	97.9(1)	96.034
C(17)-Re(1)-N(1)	92.5(1)	93.597
C(18)-Re(1)-N(1)	175.4(1)	175.575
C(16)-Re(1)-N(2)	171.2(1)	170.290
C(17)-Re(1)-N(2)	96.0(1)	89.435
C(18)-Re(1)-N(2)	101.3(1)	102.886
N(1)-Re(1)-N(2)	74.7(1)	74.265
C(16)-Re(1)-Br(1)	92.7(1)	90.399
C(17)-Re(1)-Br(1)	177.6(1)	176.076
C(18)-Re(1)-Br(1)	91.6(1)	94.069
N(1)-Re(1)-Br(1)	85.74(7)	82.555
N(2)-Re(1)-Br(1)	82.07(7)	88.780
O(1)-C(16)-Re(1)	178.6(3)	178.270
O(2)-C(17)-Re(1)	179.5(3)	179.355
O(3)-C(18)-Re(1)	179.9(3)	176.781
Selected Torsions (deg)		
N(1)-C(6)-C(1)-N(2)	-15.4(4)	-14.749
N(2)-C(5)-C(11)-N(3)	141.1(3)	136.119

Table 2.5 Selected Distances, Angles, and Torsions for **5**

	Axial CN			Planar CN	
Bond	Distance (Å)		Bond	Distance (Å)	
	Exp.	Calc.		Exp.	Calc.
Re(2)-C(35)	2.148(7)	2.13963	Re(1)-C(19)	2.105(8)	1.98769
Re(2)-C(36)	1.926(6)	1.94011	Re(1)-C(16)	1.928(5)	2.09197
Re(2)-C(37)	1.954(7)	1.96758	Re(1)-C(18)	1.96(1)	2.00792
Re(2)-C(38)	1.902(9)	1.91853	Re(1)-C(17)	1.918(7)	1.90499
Re(2)-N(5)	2.242(7)	2.28998	Re(1)-N(1)	2.253(5)	2.32197
Re(2)-N(6)	2.168(5)	2.20279	Re(1)-N(2)	2.176(4)	2.18806
C(35)-N(8)	1.138(9)	1.16104	C(19)-O(3)	1.17(1)	1.14703
C(36)-O(4)	1.145(8)	1.15044	C(16)-N(4)	1.149(7)	1.16100
C(37)-O(5)	1.151(9)	1.15134	C(18)-O(2)	1.14(1)	1.14276
C(38)-O(6)	1.17(1)	1.15368	C(17)-O(1)	1.130(8)	1.15781
Angle	Degrees (°)		Angle	Degrees (°)	
	Exp.	Calc.		Exp.	Calc.
C(36)-Re(2)-C(38)	87.7(3)	87.273	C(16)-Re(1)-C(17)	87.8(3)	90.158
C(36)-Re(2)-C(37)	88.0(3)	89.890	C(16)-Re(1)-C(18)	87.0(3)	84.822
C(36)-Re(2)-C(35)	92.1(3)	93.356	C(16)-Re(1)-C(19)	92.5(3)	88.356
C(38)-Re(2)-C(37)	88.5(3)	90.973	C(17)-Re(1)-C(18)	88.7(3)	88.453
C(38)-Re(2)-C(35)	90.8(3)	91.628	C(17)-Re(1)-C(19)	90.5(3)	87.745
C(37)-Re(2)-C(35)	179.2(3)	175.933	C(18)-Re(1)-C(19)	179.1(3)	172.179
C(36)-Re(2)-N(5)	100.6(3)	102.576	C(16)-Re(1)-N(1)	102.2(2)	98.105
C(36)-Re(2)-N(6)	174.2(3)	175.708	C(16)-Re(1)-N(2)	175.9(2)	172.047
C(38)-Re(2)-N(5)	169.3(3)	170.146	C(17)-Re(1)-N(1)	168.3(3)	170.509
C(38)-Re(2)-N(6)	96.6(3)	96.171	C(17)-Re(1)-N(2)	95.9(3)	97.544
C(37)-Re(2)-N(5)	98.4(2)	89.360	C(18)-Re(1)-N(1)	97.7(3)	88.487
C(37)-Re(2)-N(6)	96.0(2)	92.605	C(18)-Re(1)-N(2)	94.8(3)	93.374
C(35)-Re(2)-N(5)	82.3(2)	87.543	C(19)-Re(1)-N(1)	83.2(2)	96.317
C(35)-Re(2)-N(6)	83.9(2)	84.008	C(19)-Re(1)-N(2)	85.7(2)	93.899
N(5)-Re(2)-N(6)	74.7(2)	73.977	N(1)-Re(1)-N(2)	73.9(2)	73.675
O(6)-C(38)-Re(2)	179.4(7)	178.027	O(1)-C(17)-Re(1)	178.2(7)	177.623
O(5)-C(37)-Re(2)	175.5(6)	179.414	O(2)-C(18)-Re(1)	172.0(7)	176.452
N(8)-C(35)-Re(2)	178.0(6)	176.457	O(3)-C(19)-Re(1)	178.0(6)	176.552
O(4)-C(36)-Re(2)	179.0(7)	177.313	N(4)-C(16)-Re(1)	178.7(6)	178.113
Torsion	Degrees (°)		Torsion	Degrees (°)	
	Exp.	Calc.		Exp.	Calc.
N(5)-C(20)-C(25)-N(6)	14.5(9)	13.735	N(1)-C(1)-C(6)-N(2)	12.5(8)	14.777
N(5)-C(24)-C(30)-N(7)	41(1)	135.774	N(1)-C(5)-C(11)-N(3)	43.7(9)	137.014

Structural comparisons between the bidentate samples and the terdentate show many similarities. The loss of one carbonyl always accompanies the dentation of the pendant arm of the ligand. The increased coordination forces the ligand to adopt a more rigidly planar geometry, this is visible in the structure of **2.2** (Figure 2.8a) and **2.8** (Figure 2.8b). Structures for other discusses species were unable to be collected.

(a) X-ray crystal structure for **2.2**   (b) X-ray crystal structure for **2.8**
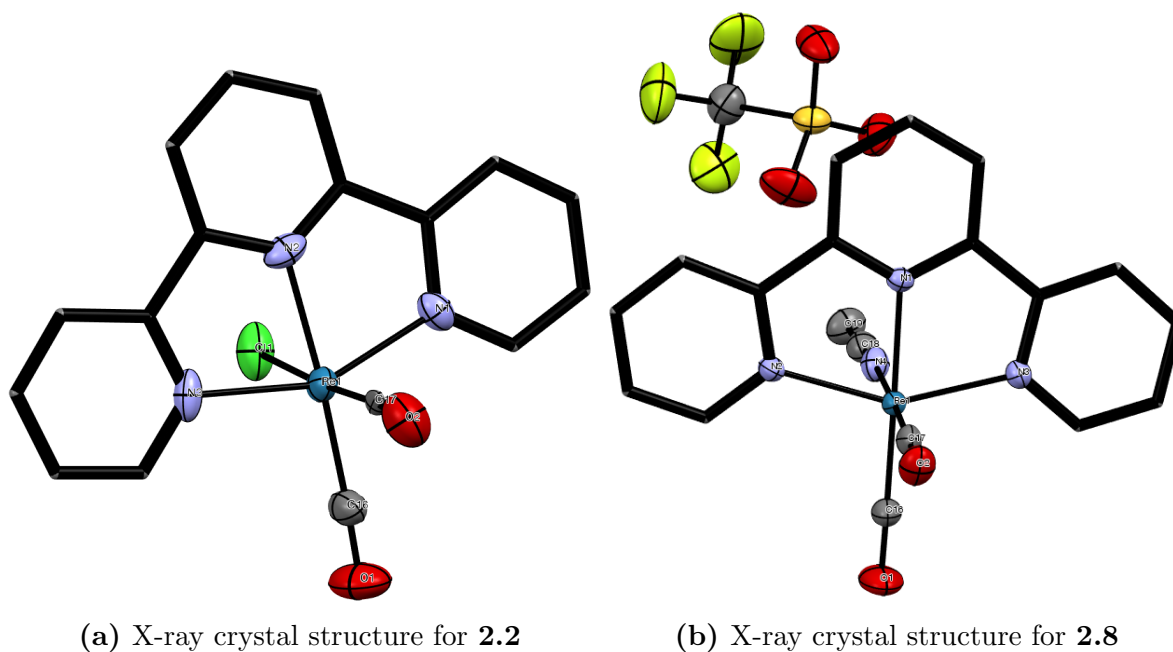
Figure 2.8 X-ray crystal structure representation for **2.2** and **2.8**. Co-crystallized chloroform, hydrogen atoms, and thermal ellipsoids of ligand carbon atoms are omitted for clarity.

Selected bond lengths, bond angles, and torsions are listed in Table 2.6 and Table 2.7 for products **2.2** and **2.8**. Cell parameters and collection data can be found in Table 2.8.

not done

Table 2.6 Selected Distances, Angles, and Torsions for **2**

Bond	Distance (Å)	
	Experimental	Calculated
Re(1)-C(16)	1.926(9)	1.92438
Re(1)-C(17)	1.975(10)	1.90687
Re(1)-N(1)	2.119(7)	2.13186
Re(1)-N(2)	2.080(7)	2.08705
Re(1)-N(3)	2.126(7)	2.13185
Re(1)-Cl(1)	2.489(3)	2.53337
N(1)-N(3)	4.14(1)	4.14772

Angle	Degrees (°)	
	Experimental	Calculated
C(16)-Re(1)-C(17)	91.5(4)	89.188
C(16)-Re(1)-N(2)	173.7(4)	172.050
C(17)-Re(1)-N(2)	94.6(3)	98.762
C(16)-Re(1)-N(1)	103.9(3)	102.980
C(17)-Re(1)-N(1)	92.7(3)	93.429
N(2)-Re(1)-N(1)	77.3(3)	76.684
C(16)-Re(1)-N(3)	101.8(3)	102.986
C(17)-Re(1)-N(3)	91.7(3)	93.419
N(2)-Re(1)-N(3)	76.6(3)	76.684
N(1)-Re(1)-N(3)	153.7(3)	153.210
C(16)-Re(1)-Cl(1)	91.8(3)	89.136
C(17)-Re(1)-Cl(1)	176.5(2)	178.324
N(2)-Re(1)-Cl(1)	82.1(2)	82.913
N(1)-Re(1)-Cl(1)	85.4(2)	86.953
N(3)-Re(1)-Cl(1)	88.7(2)	86.953
O(1)-C(16)-Re(1)	177.9(9)	179.079
O(2)-C(17)-Re(1)	173.2(8)	179.182

Selected Torsions (deg)		
N(1)-C(5)-C(6)-N(2)	1(1)	2
N(2)-C(10)-C(11)-N(3)	-4(1)	-2

Table 2.7 Selected Distances, Angles and Torsions for Acetonitrile Adduct of **8**

Bond	Distance (Å)	
	Experimental	Calculated
Re(1)-C(16)	1.889(4)	1.92288
Re(1)-C(17)	1.885(3)	1.92394
Re(1)-N(1)	2.091(3)	2.10787
Re(1)-N(2)	2.135(3)	2.15342
Re(1)-N(3)	2.131(3)	2.16262
Re(1)-N(4)	2.160(3)	2.14739
N(2)-N(3)	4.138(4)	4.19048

Angle	Degrees (°)	
	Experimental	Calculated
C(16)-Re(1)-C(17)	87.69(16)	
C(16)-Re(1)-N(1)	175.95(12)	
C(17)-Re(1)-N(1)	96.35(12)	
C(16)-Re(1)-N(3)	103.81(13)	
C(17)-Re(1)-N(3)	94.03(12)	
N(1)-Re(1)-N(3)	76.20(10)	
C(16)-Re(1)-N(2)	103.58(13)	
C(17)-Re(1)-N(2)	93.73(12)	
N(1)-Re(1)-N(2)	75.99(10)	
N(3)-Re(1)-N(2)	151.77(11)	
C(16)-Re(1)-N(4)	90.50(14)	
C(17)-Re(1)-N(4)	178.10(12)	
N(1)-Re(1)-N(4)	85.46(10)	89.737
N(3)-Re(1)-N(4)	86.94(10)	
N(2)-Re(1)-N(4)	86.15(10)	86.044
O(1)-C(16)-Re(1)	179.1(3)	178.587
O(2)-C(17)-Re(1)	178.0(3)	178.820

Torsion	Degrees (°)	
	Experimental	Calculated
N(1)-C(1)-C(6)-N(2)	1.7(4)	-1.3
N(1)-C(5)-C(11)-N(3)	-1.8(4)	-0.3

Table 2.8 Crystal data and structure refinement for compounds **2**, **4**, **6**, and **8**

Compound	2	4	6	8
Empirical formula	$C_{18}H_{11}N_3O_2ReCl$	$C_{18}H_{11}N_3O_2ReBr$	$C_{19}H_{11}N_4O_2Re$	$C_{21}H_{14}N_4O_5F_3SRe$
Formula weight (g/mol)	510.95	530.04	502.04	665.61
Temperature (K)	200(2)	200	200	200
Wavelength (Å)	0.71073	0.71073	0.71073	0.71073
Crystal System	Triclinic			Triclinic
Space Group	P-1			P-1
a (Å)	8.5275(3)			8.5745(4)
b (Å)	14.2421(5)			11.9805(5)
c (Å)	17.4637(6)			13.0970(5)
α (deg)	77.948(2)			79.748(2)
β (deg)	85.684(2)			81.106(2)
γ (deg)	79.890			88.091(2)
Volume (Å^3)	2041.79(12)			1307.99(10)
Z, r (calc) (Mg/m^3)	4, 2.050			2, 1.993
Absorption coefficient (mm^{-1})	6.494			5.094
Absorption correction		Semi-empirical from equivalents		
Final R indices [I$\geq 2\sigma$(I)]	R1 = 0.0636, wR2 = 0.1018			R1 = 0.0294, wR2 = 0.0673
R indices (all data)	R1 = 0.0985, wR2 = 0.1110			R1 = 0.0366, wR2 = 0.0700

2.3.3 Infrared Spectroscopy

Conversion of bidenate to terdentate species was confirmed utilizing Fourier Transform Infrared (FTIR) spectroscopy. A small sample of powder product was placed on the Agilent Cary 630 FTIR spectrometer, with a 2 cm^{-1} resolution. The instrument is fitted with a diamond ATR for solid sample analysis. Spectra are the Fourier transform of 16 scans.

Analysis of the results in Figure 2.9 shows the significant reduction of one peak in the (ca.) 2100 cm^{-1} region. This peak is in the CO stretching frequency, the frequency of the peak lost in thermolysis is indicative of a weakly coordinated carbonyl group. A splitting occurs for the other large peak and its shoulder in the conversion from bidentate to terdentate, from 1890 to 1790 cm^{-1}, indicating the further weakening of the metal carbonyl bonds remaining in the complex. This weakened bond is likely the carbonyl co-planar to the ligand, analysis of the x-ray crystal structure shows the CO bond to be
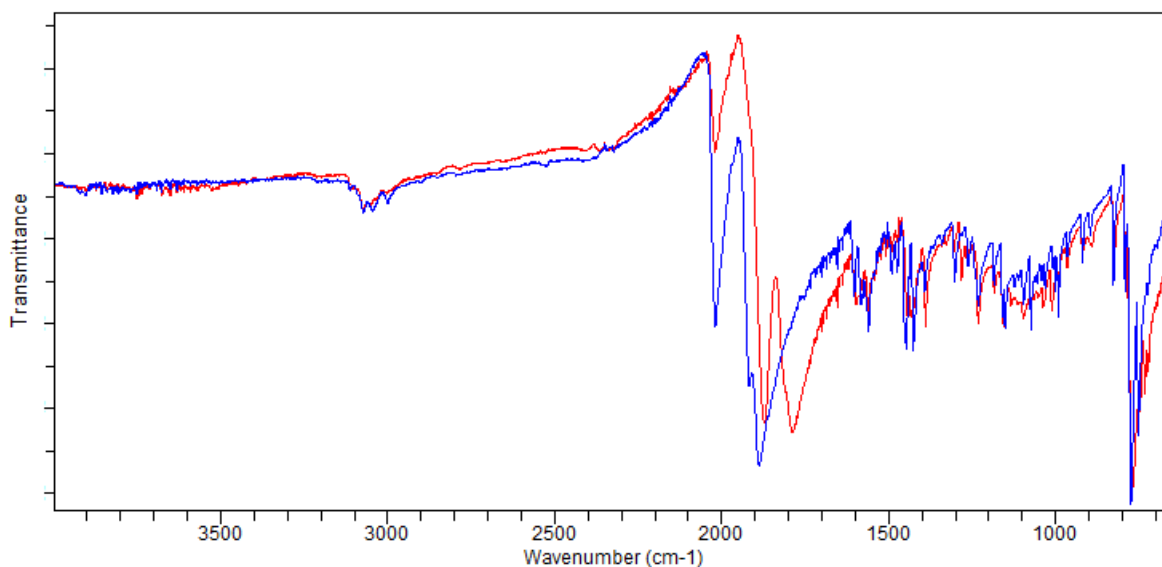
Figure 2.9 FTIR Spectra for complexes **2.1** (blue) and **2.2** (red).

0.1 Å longer than that of the axial carbonyl. This agrees with DFT predicted IR spectra, in which the charactaristic triple peak is reduced to a double peak, in association with the shift to lower energy of one carbonyl stretching frequency (associated to the carbonyl.

FTIR spectra were predicted using molecular frequency calculations of DFT optimized structures in Gaussian09. Prediction of this spectra was performed as a verification of the optimized structures discussed in subsection 2.3.2 above. The calculation identifies stretching or bending harmonic energies in optimized structures. The computed spectra in **??** shows three peaks for **2.1**, at 2094, 2012, and 1990 cm^{-1}. The relative location of these peaks corresponds to those seen in Figure 2.10 for **2.1**, but are shifted by approximately 100 cm^{-1} to higher energy relative to the experimental. Similarly, for **2.2**, peaks are seen at 2000 and 1950 cm^{-1}, compared to the 1890 and 1790 peaks seen experimentally. This computed value reflects the shift to lower energy carbonyl stretching from **2.1** to **2.2**, and echoes the experimental spectra well.

Further analysis of other spectra were not successful in identification of any additional

axial or equatorial

look up computated spectra and double check frequency peaks
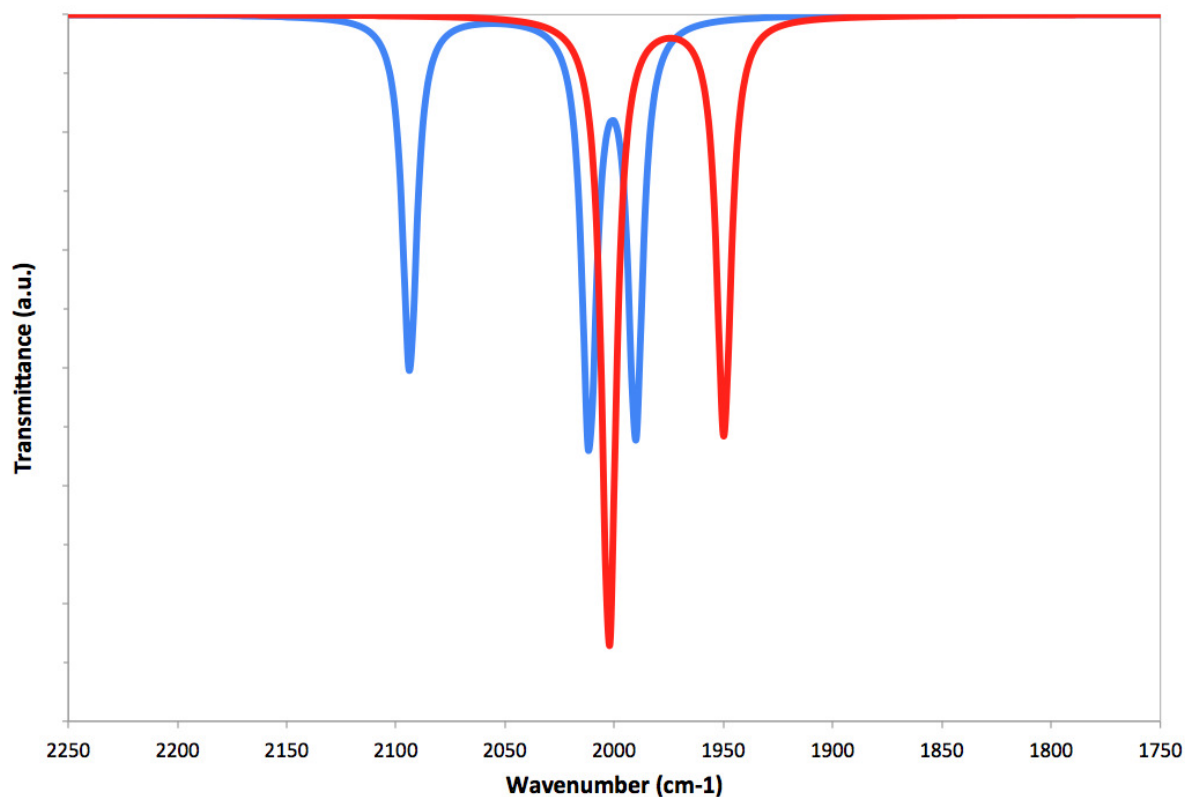
Figure 2.10 DFT predicted FTIR spectra for **2.1** (blue) and **2.2** (red).

molecular properties, with the exception of a series of strong peaks appearing in the 1200-1300 cm^{-1} range, confirming the presence of the triflate anion from the -SO$_3$ group vibrations for samples **2.7** and **2.8** (Figure 2.11). Additionally, the small peak present at 2270 cm^{-1} in the terdentate sample corresponds to the weakly coordinated acetonitrile occupying the moluecule's axial position.
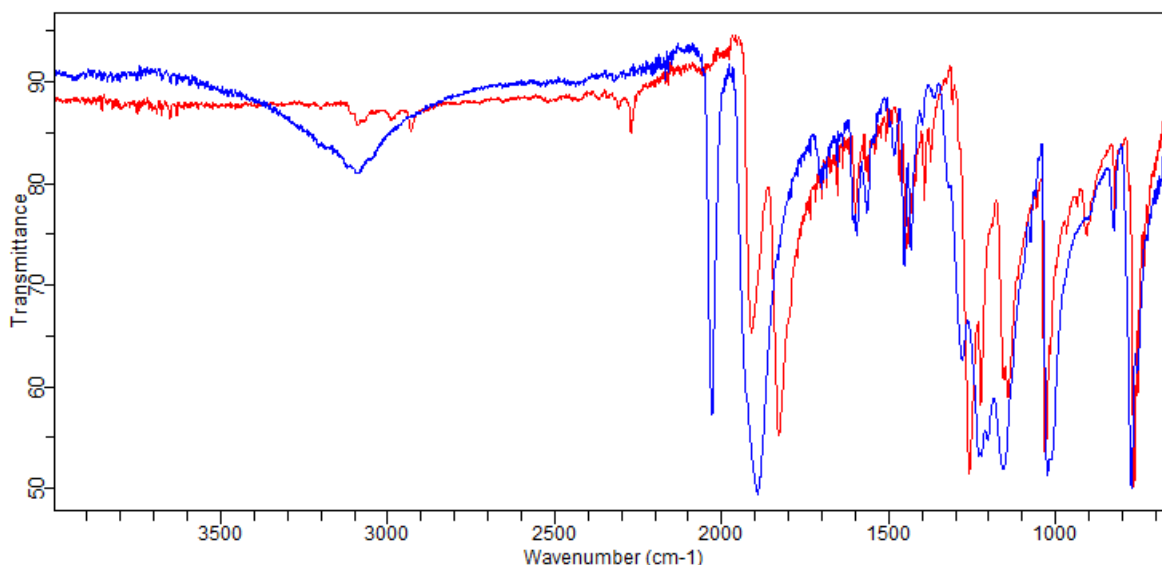
Figure 2.11 FTIR Spectra for complexes **2.7** (blue) and **2.8** (red).

2.3.4 Photophysical Properties

A striking observation upon the conversion of the bidentate species into the terdentate complexes is that these new compounds have a substantially darker colour that reflects a significant change in the photophysical properties. This effect was investigated using a combination of UV-visible spectroscopy and DFT modelling. Spectra were collected on a Agilent Cary 5000 UV-Vis-NIR Spectrophotometer. The stronger absorbance of the terdentate complexes compared to the bidentate precoursors is evident in the UV-Vis spectra of these species, and is presented in Figure 2.12. These spectra were obtained in Dimethylsulfoxide (DMSO) with approximate concetrations of 0.01 mM for bidentate, and an order of magnitude lower (0.001 mM) for the terdentate analogues. The terdentate complexes have more intense absorbance for higher energy ligand UV-based π-π^* transitions (<400 nm) and certainly a richer visible absorption profile that involve the d-π^* transitions. These features are responsible for the colour change observed.

The UV-Vis spectra were modeled using TD-DFT computations within Gaussian 09,
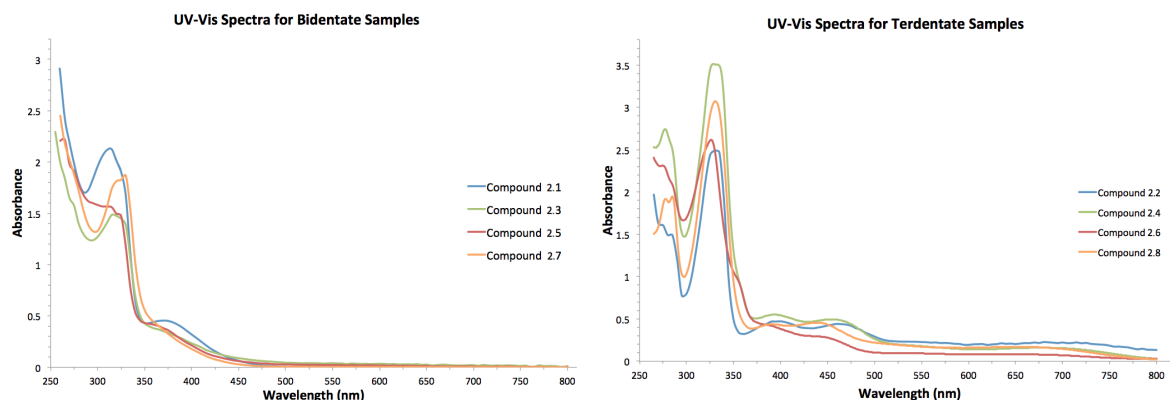
(a) UV-Vis spectra for compounds **2.1**, **2.3**, **2.5**, and **2.7**

(b) UV-Vis spectra for compounds **2.2**, **2.4**, **2.6**, and **2.8**

Figure 2.12 UV-Vis spectra for all compounds. Concentrations of bidentate complexes are 0.01 mM and terdentate complexes are 0.001 mM.

using the B3LYP functional with the LanL2DZ basis set and effective core potentials for the rhenium atom, and the TZVP basis set for all lighter atoms. Such functional and basis set choices are common within organometallic literature. Solvent was simulated using the integral equation formalizm variant of the PCM solvation model, with DMSO as the solvent.

The resulting computed spectra were excellent matches to the experimental spectra. The similarity of the spectra between the bidentate species and as well as the terdentate species indicates that parallel electronic transitions appear within these two groups. Specifics will be discussed for the chloro compounds, **2.1** and **2.2**, but strong parallels exist for all species. Plots of experimental and computational data for these two complexes are presented in Figure 2.13 and Figure 2.14, respectively.

Common to all bidentate compounds were peaks at wavelengths of 315-320 nm, and peak shoulders near 350-375 nm (Figure 2.12a). In the case of **2.1**, the computational results suggest that the experimental band centred at λ = 315-320 nm (31750-31250 cm^{-1}) primarily arises from two electronic transitions. The first is from HOMO-3 to
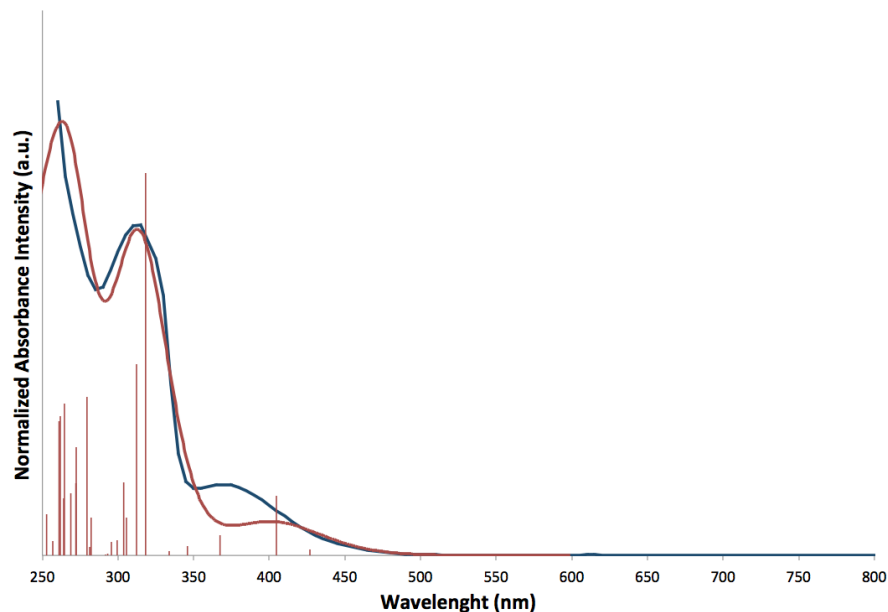
Figure 2.13 Plots of the experimental and computed UV-Vis spectra for compound **2.1**. The blue curve shows experimental result.The red vertical lines show the calculated transitions and relative intensities from the TDDFT calculations, while the red curve shows the Gauss convolution with peak width at half height of 0.250 eV.

LUMO, a π-π^* transition, while the second major contribution is the excitation from HOMO to LUMO+2, which is a d-π^* transition. The TD-DFT calculations suggest that the experimental band centred at $\lambda = 370$ nm (27030 cm^{-1}) corresponds to a calculated transition at approximately 400 nm, that is a d-π^* (HOMO-1 to LUMO) absorbance. Computed plots of molecular orbitals are included in Appendix B Molecular Orbitals and Energy Diagrams.

Like the bidentate samples, the spectra for the terdentate samples are quite similar to one another. In general, all of these species have much higher absorbance coefficients than their bidentate analogues; all contain long trailing absorptions across the wavelengths analysed. For terdentate complex **2.2**, the four experimentally observed UV-Vis absorptions observed are made up of six computed transitions. The computational model provided two equal and strong tranitions appearing at 308 and 325 nm to generate the
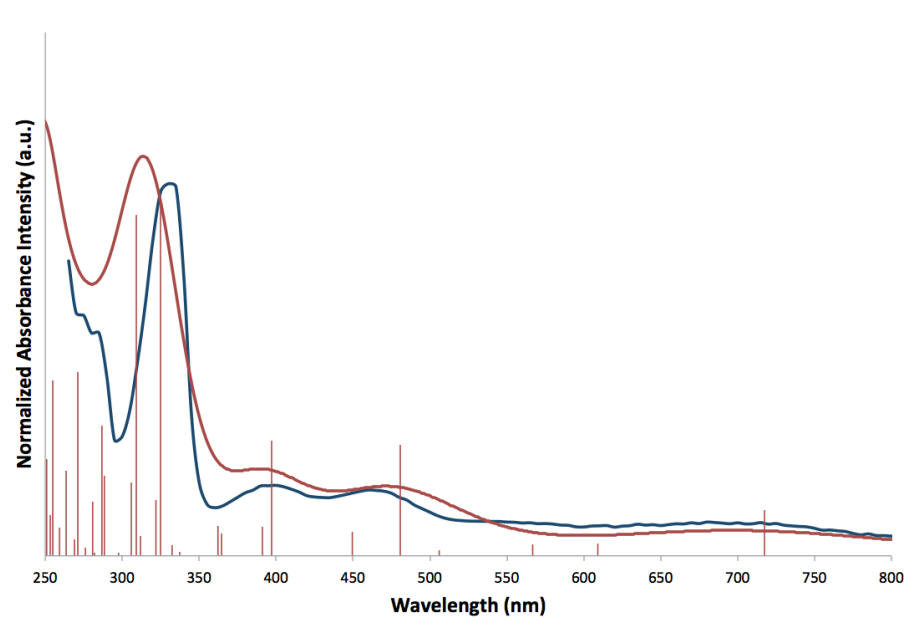
Figure 2.14 Plots of the experimental and computed UV-Vis spectra for compound **2.2**. The blue curve shows experimental result.The red vertical lines show the calculated transitions and relative intensities from the TDDFT calculations, while the red curve shows the Gauss convolution with peak width at half height of 0.250 eV.

experimental band centred at $\lambda = 330$ nm (30300 cm^{-1}). These arise from a transition from HOMO-5, to LUMO, a Cl lone-pair to terpy π^*-orbital absorption, and from HOMO-3 to LUMO, which is a ligand centred π-π^* transition. All of the lower energy transitions are dominated by MLCT bands. The experimental band centered at $\lambda = 400$ nm (25000 cm^{-1}) arises from an electronic transition from HOMO to LUMO+3 which is d-π^* in nature. The absorbance centred at $\lambda = 460$ nm (21740 cm^{-1}) corresponds to two MLCT d-π^* transitions; HOMO-2 to LUMO and HOMO-1 to LUMO+1. Finally, the broad experimental band 680-715 nm (14700-14000 cm^{-1}) arises from the electronic transition appearing at 718 nm, which is the excitation of a d-electron in the Re-centered HOMO to the ligand π^* LUMO.

2.3.5 Fluorescence

Fluorescence data was collected for **2.1** and **2.2** using an Agilent Cary Eclipse Fluorescence Spectrophotometer, using a 5 nm excitation slit and emission slit, using excitation wavelengths selected to correspond to the centre of UV-Vis absorption bands. Data was collected for spectra in N,N-dimethylformamide (DMF) to simulate the photocatalytic reaction environment (see chapter 3). Spectra are shown in Figure 2.15 for **2.1** and **2.2** with their UV-Vis absorption spectra for comparison. Data is normalized to equil concentration for each sample in fluorescence and absorbance.
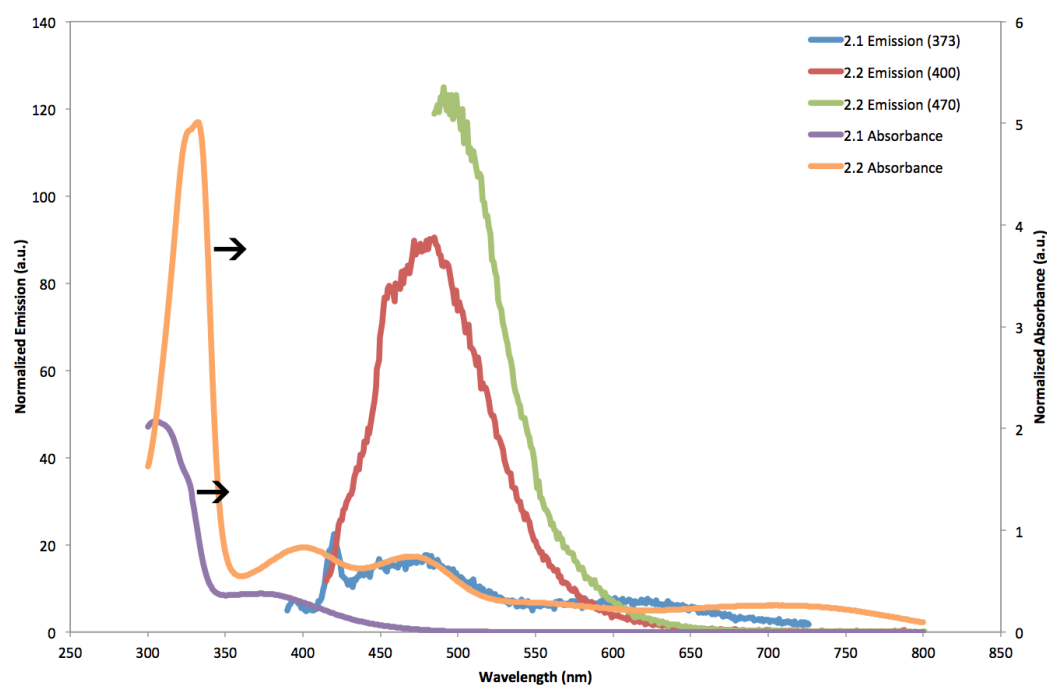
Figure 2.15 UV-Vis and fluorescence spectra for **2.1** and **2.2**. Fluorescence of **2.1** from excitation of 373 nm (blue), excitation of **2.2** by 400 nm (red) and 470 nm (green) are shown, along with the absorption spectra of **2.1** (purple) and **2.2** (orange).

Clearly the transformation from bidentate terpyridine to terdentate ligand has significant effect on the interactions of these Re compounds with visible light. Terdentate samples fluoresce and absorb more intensely at lower energy wavelengths. While the

terdentate sample is excited at various wavelengths (that should correspond to different absorption bands), the emission appears to be from one single band centred at ca. 490 nm.

Interestingly, emission is not seen with the naked eye with 400 nm excitation for the terdentate, while the bidentate emission is very strong. This may be due to self-absorbance in the terdentate samples, emission of 490 nm is easily absorbed by the molecule. In the bidentate, no absorbance bands correspond with emission seen at 470 nm or 600 nm, these appear to the naked eye as a white emission.

2.4   Conclusions

This work reported the first crystallographically authenticated rhenium(I) terpyridine terdentate complexes and thus expanded upon the prior limitations of Re coordination complexes. These terpyridine complexes are accessed via a simple, highly efficient, solid-state thermolysis pathway. They expand upon the known α-diimine photophysical properties, with enhanced metal-to-ligand d-π^* electronic transitions, occurring more frequently and with lower energy than in the associated bidentate compounds. These observations are supported by computational TD-DFT results, affording an expanded understanding of the transition bands. Modification of the bidentate and terdentate species has been shown, the synthetic success of a triflate moiety should facilitate further development of reactivity and provides an opportunity for synthetic and catalytic studies.

Chapter 3

Photocatalysis of CO$_2$

3.1 Introduction

Only 6 years after Re$^\text{I}$ complexes using 2,2'-bipyridine were characterized, Hawecker,
Ziessel, and Lehn showed the effectiveness of the compound for the photocatalytic re-
duction of CO$_2$.[59] Since then, many have shown the efficacy of a wide range of α-diimino
complexes for the reaction, and expansion of the systems to bimetallic complexes with
ruthenium and osmium as electron transfer agents has produced a wide range of results.
The mechanism of reduction has been subject of some debate: while mechanisms have
been proposed since Lehn et. al. soon after their original publication,[60] modifications
have been submitted routinely over the past decades. Further discussion and a proposal
of a new mechanism geometry based on computational and experimental data can be
read in chapter 4.

check ref
names

a few refer-
ences

refer to these
as well. Red
Light paper?

references,
Morris, JACS
dimer, mech.
basis

3.2 Photocatalytic Reactions with New Compounds

The photocatalytic cycle is, simply, a photon-induced MLCT, followed by the extraction of an electron from a sacrificial reductant. This radical, negatively charged species sheds the anion, opening up a reaction site. Reaction between a CO_2, a proton (from the decomposition of the reductant or elsewhere), and the catalyst yields any number of CO, H_2O, formate (HCO_2^-), or carbonate (CO_3H^-), depending on the mechanistic pathway.

3.2.1 Conditions

Reaction conditions in use in literature have remained typically unchanged since the original papers. A mixture of DMF with either Triethanolamine (TEOA) or Triethylamine (TEA) at a 5:1 ratio is used to make a 1.0 mM solution of catalyst, with 'excess' (depending on reference, a 1.1 to 25 molar ratio) electrolyte salt (typically Et_4NX or t-Bu_4NX, where X = halide from catalyst) added as a stabilizer. Solutions are degassed by bubbling of CO_2 and a consistent headspace is left to form over the solution. The reaction is monitored via Gas Chromatography (GC) analysis of the headspace, using a HP gas chromatograph with a 15 m CARBONPLOT column with 0.320 mm inner diameter and 1.50 μm film in a 40°C oven. The instrument is fitted with a Thermal Conductivity Detector (TCD), and, while using He as a carrier gas, is able to resolve CO and CO_2 completely.

3.2.2 Experimental Results

Both bidentate and terdentate κ^n(terpy)Re(CO)$_{5-n}$X (n=2, 3) **2.1** and **2.2** complexes show no activity for CO_2 reduction. Modification of testing time, light source, product analysis methods, solvent, sacrificial reductant, pH, presence of electrolyte, presence of

H$_2$O, or variation of anion (X=Cl, Br, OTf, CN) shows no change of this inactivity. Testing of κ^2(bipy)Re(CO)$_3$Cl under the same reaction and testing conditions shows production of approximately 6 mL CO from CO$_2$ (20% conversion) in 1 hour of photolysis with visible (λ >400 nm) light, verifying the method, isolating the catalyst as the ineffective species.

3.2.3 Rationalization of Results

TEOA insertion, maybe clear is a acid, formate, carbonate, tricarbonylcation or other complex?

reference

Examples in literature show the requirement for fluorescence for successful catalytic candidates. The explanation for this is the requirement for a stable, long-lasting excited state, with lifetime greater than that of the timescale required for electron abstraction from the sacrificial amine. The observed fluorescence demonstrates the lack of non-radiative relaxation pathways, considered to be an analogue for the extended lifetime of the excited state. Sample **2.2** shows only poor fluorescence. While the complex is able to absorb light across the spectrum, and has HOMO to LUMO transitions with high enough energy[i] for the catalyzed reduction of CO$_2$ to CO, it appears as if the catalysis is not initiated due to a short excited state lifetime. Fluorescence data presented in New Coordination Geometries for Re$^{\text{I}}$, at subsection 2.3.5 shows the lack of fluorescence in terdentate samples **2.2** and **2.4**.

Explanation for the lack of CO production observed in the attempted photochemical reduction of CO$_2$ by bidentate sample **2.1** and others must come from another angle. These samples are quite fluorescent, emission from the powder sample can be seen with the naked eye with simulation by a 405 nm laser pen under ambient light environments. Importantly, two clues come from the reaction mixture: under intense visible light in the

---

[i]Electrochemical reduction in similar environments takes 1.7-2.1 V, equivalent to HOMO-LUMO transitions from 590-750 nm.[81]

presence of CO$_2$ the compound bleaches to a very faint yellow-green and colour does not return after storage in the dark, bubbling of new CO$_2$, or other manipulations. Secondly, a mixture of sacrificial amine, DMF, Et$_4$NCl, and catalyst **2.1** in ratios identical to what is required in the reaction mixture changes colour from a yellow to a deep red irreversibly after 5 days at ambient temperature, both in dark or under ambient light.

3.1
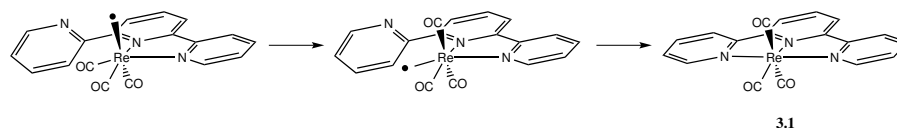
Scheme 3.1 Formation of **3.1** from catalytic excimer via reorganization of carbonyls and chelation of the pendant arm.

These variations provide some opportunity for identifying methods of deactivation. The bleaching (formation of a very pale yellow-green to clear species) may be due to the loss of the halide, followed by carbonyl reorganization and pendant arm complexation to form **3.1**, see **??**. This scheme is available to the mechanism via well known processes, lability of carbonyl groups around a metalc entre is well established. The resulting compound, $[\kappa^3-(\text{terpy})-\text{Re}(\text{CO})_3]^+$, appears to not have been isolated in literature previously, direct comparisons to experimental colour or UV-Vis is not possible. However, TD-DFT calculations with the same parameters used in chapter 2 (B3LYP functional, with a mixed LanL2DZ and TZVP basis set) demonstrate an absorption spectra with very little visible contributions, shown in Figure 3.1. This corresponds to the bleached appearance of the reaction mixture.

Figure 3.1 Computational structure (inset) and predicted UV-Vis absorption spectra of $[\kappa^3-(\text{terpy})-\text{Re}(\text{CO})_3]^+$

Chapter 4

Mechanism of CO$_2$ Reduction

4.1 Introduction

Within three years of the appearance of the originally reported bipyridine rhenium (I) catalyst, experimental studies on the mechanism of the photocatalytic reduction of CO$_2$ were available in the literature.[60] Studies continue on the mechanism up to the present day,[82–86] utilizing new investigative techniques as they become available to elucidate transition states and transient intermediates *in situ.*

Investigation includes the use of DFT methods to elucidate geometries of intermediates and transition states for of the multi-step cycle. Transition metal catalysis is a non-trivial problem computationally, particularly when considering a metal from the lower period. These elements contain a large amount of electrons, many of which can be involved in non-covalent interactions with the ligands and catalyzed products. Solving for this complex system becomes non-trivial and computationally expensive. For this reason, no overview of the mechanism as investigated by DFT methods has ever been made available in the literature.

4.2 Literature Mechanism Pathways

Prior work in the literature has proposed three general mechanistic pathways for the photoreduction of CO_2. In general, as seen in Figure 4.1, these pathways result in the formation of CO and H_2O, formate (HCO_2^-), or carbonate (CO_3H^-) anions. The formation of carbonate proceeds via the formation of a catalyst dimer over a molecule of CO_2, with the insertion of a second molecule of CO_2 to produce the carbonate and a molecule of CO. Production of formate occurs via insertion of CO_2 to a rhenium hydride bond. The formation of CO without carbonate or formate by-products occurs via the coordination of CO_2 to an open site on the metal, followed by a double proton addition and the release of a molecule of H_2O prior to the loss of one of the four carbonyl groups to open up the axial site for halide re-coordination. This is essentially the Reverse Water-Gas Shift Reaction (RWGSR), wherein protons are made available from decomposition of the sacrificial amine instead of from decomposition of H_2.[87] These three mechanistic pathways will be referred to as the 'carbonate' mechanism, the 'formate' mechanism, and the 'water-gas shift' mechanism, respectively.

Each of the mechanistic pathways identified above in Figure 4.1 was studied, using DFT methods. Structures (using 2,2'-bipyridine as the bidentate ligand, and triethylamine as the sacrificial reductant) were optimized to ground or transition states using TurboMole 6.5,[88,89] with the TPSS meta-GGA XC functional.[90] The def2-TZVP basis set was used for all atoms.[76,91] The TurboMole program contains a number of optimizations to the original DFT algorithms,[92–100] decreasing the calculation time without compromising accuracy. Grimme's dispersion correction (version 3) was included in the calculations.[101] Intermediates and transition states were verified by frequency analysis,[97,102,103] with further verification of transition states by performing dynamic reaction coordinate calculations to determine the Intrinsic Reaction Coordinates (IRCs). The effects of sol-

Figure 4.1 An overview of the mechanistic pathways of photochemical CO$_2$ reduction. Catalyst is shown in blue, and the excimer species in red

vation was calculated using the Conductor-like Screening Model (COSMO) implemented in TurboMole,[104] which is a continuum solvation model implicitly surrounding the solute molecule. Code was developed to assist with managing the computational jobs (see chapter 5).

Refs. Sullivan and Gilbert

refs

Many of the intermediates have been synthesized in various studies , indicating their reasonable stability. While individual portions of the mechanism have been studied computationally in the past[105–107], no over-arching study has compared methods relative to each other. Furthermore, while the formation of CO with H$_2$O is the most anticipated pathway (due to the lack of formation of carbonate or formate in most studies), no literature pathway exists to explain the addition of CO$_2$ to the open site of the radical catalytic species without a three body reaction step (catalyst, CO$_2$ and H$^+$ together) or

without formate reorganization. Furthermore, no mechanism proposed thus far explains the [12]CO to [13]CO isotopic exchange demonstrated by Lehn's group in 1986.[60]

4.2.1 Eximer Formation and Decomposition of the Sacrificial Amine

All of the pathways require the formation of a common eximer, namely, the radical $17e^-$ species (Figure 4.2). This occurs through the absorption of an incident photon with enough energy to promote an electron from the metal d-orbital to the ligand π^* orbitals in the ground state catalyst, **4.01**, forming the triplet Metal-Ligand Charge Transfer (3-MLCT) complex **4.01** [3]. The pseudo-oxidized, electron-deficient metal atom extracts an electron from the sacrificial amine present in the reaction solution to return to the Re^I state (**4.02**). However, this complex is formally a radical anion, the halide (**4.04**) is lost to return to the neutral eximer species in solution, **4.03**. This extraction to form the radical anion catalyst and the radical cation amine is thermodynamically expensive, costing 47.60 kcal/mol in DMF and nearly 125 kcal/mol in the gas phase. The difference in energies demonstrates the importance of performing calculations in a simulated solution; steps that may have insurmountable energy barriers in the gas phase become possible once solvation is considered.

values of 3MLCT

A slight uphill to dissociation of the chloride (15.44 kcal/mol in DMF) allows for the formation of the triplet $17\ e^-$ excimer species **4.03**, from which the following mechanism pathways may diverge. It is important to note that some studies suggest the solvent coordinates with the excimer species.[86,108] This solvent coordination is expected to stabilize the excimer species prior to reaction with CO_2 in solution. However, this event has no bearing on the overall reaction energies, the coordination and subsequent loss of solvent is an energetically neutral occurrence and was not studied in detail.
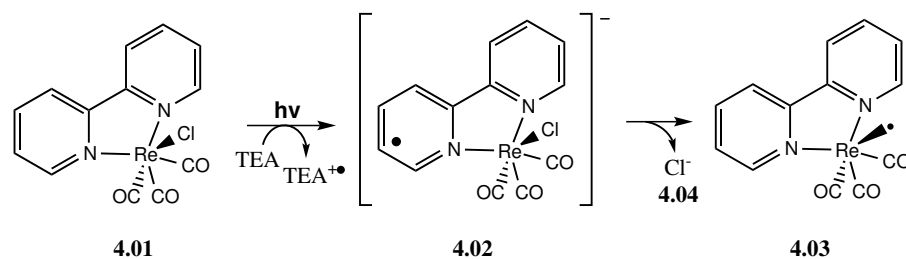
Figure 4.2 Formation of the eximer species via absorption of a photon and oxidation of the sacrificial amine.

The decomposition of the sacrificial amine was first identified by Kalyansundarem in 1978,[87] and is summarized in Figure 4.3. This work showed the route for decomposition of TEOA but the mechanism for decomposition of TEA is parallel. This decomposition is critical due to the protons it provides to the reaction mixture, and the presence of a simple second electron abstraction from the decomposition product. Upon absorption of a photon by the catalyst, the amine **4.05** is converted to the radical cationic species ($Et_3N^{+\cdot}$, **4.06**). This undergoes a proton transfer to a second molecule of the sacrificial reductant. The transfer removes a proton from the α carbon, leaving it a neutral radical species (**4.07**). This is then able to react in the catalytic cycle to provide a second electron and form the ethene-diethylamino compound. Triethylammonia is produced as well (**4.08**), this is a proton source for the formate and water-gas shift mechanistic pathways. This step is slightly exothermic, with energy releases of 1 kcal/mol in gas phase, or nearly 3 kcal/mol in DMF.

Energies of **4.01** - **4.10**, and **4.26** in gas and solution phases (in DMF) is shown in Table 4.1, along with the energy of solvation. Energies of each step of the reaction are listed in Table 4.2. The values show a significant 'uphill' series of steps requiring significant energy input. This energy is supplied by the incident photons; this process is a photocatalyzed activation. The reaction typically requires incident light of 400 nm
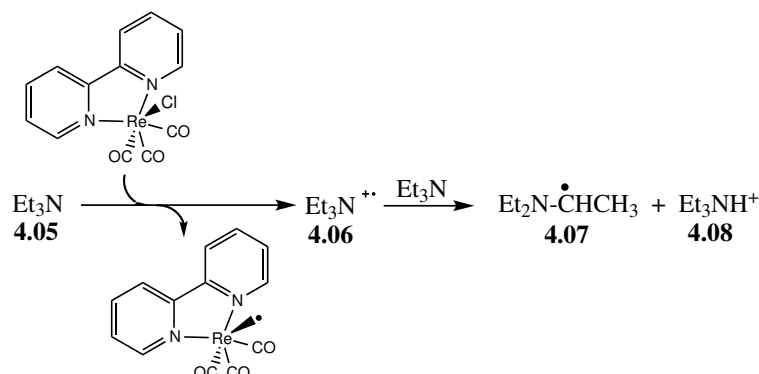
Figure 4.3 Decomposition pathway for the sacrificial amine.

energy, this significant energy input allows for the pathway to be followed.

Table 4.1 Gas phase and solvated energies of mechanism reactants and products.

Molecule	Label	E (gas)[a]	E (solution)[b]	E (solvation)[c]
Ground State	4.01	-1374.621419	-1374.651099	18.62
Radical Anion	4.02	-1374.684002	-1374.759190	47.18
Open Site Excimer	4.03	-914.3139376	-914.3287245	9.28
Chlorine Anion	4.04	-460.2890817	-460.4058583	73.28
Triethylamine (TEA)	4.05	-292.3051496	-292.3854033	50.36
Radical Cation TEA	4.06	-292.3051496	-292.3854033	50.36
Deprotonated TEA Radical	4.07	-291.9173706	-291.9211226	2.35
Triethylammonia	4.08	-292.9552538	-293.0382729	52.09
Carbon Dioxide	4.09	-188.6945676	-188.6974631	1.82
Carbon Monoxide	4.10	-113.3744946	-113.3754466	0.60
Diethylaminoethene	4.26	-291.3467768	-291.3525868	3.64

[a] TPSS SCF energy in hartrees.
[b] TPSS SCF energy in hartrees with COSMO solvation in DMF.
[c] TPSS solvation energy in kcal/mol (E(gas) - E(solution)).

Geometries of the catalyst do not change significantly throughout this transformation. Key bond lengths and angles include the ligand-Re bonds and CO-Re bonds, the addition and subtraction of electrons to and from the complex impact the bonding. As the reaction proceeds, for example, the calculated Re-N distance in solvated structures decreases from

Table 4.2 Energies for the reaction steps in the excimer formation pathway

Reaction Steps	Energy(gas)[a]	Energy(dmf)[b]
4.01 + 4.05 $\longrightarrow$ 4.02 + 4.06	124.261582	47.596907
4.02 $\longrightarrow$ 4.03 + 4.04	50.816912	15.440887
4.06 + 4.05 $\longrightarrow$ 4.07 + 4.08	-1.077024	-2.915901

[a] TPSS SCF energy in kcal/mol.
[b] TPSS SCF energy in kcal/mol with COSMO solvation in DMF.

2.18924 Å in the ground state catalyst to 2.14212 Å in the neutral radical excimer. Similarly, the distance from the metal to the axial carbonyl decreases from 1.91950 to 1.88746 Å in the same circumstances. These changes are not significant, the bond order is unchanged across these distances, but bond modification of 0.05 Å is large enough to demonstrate a change has occurred in the bonding around the metal. Subsequent steps in the mechanism demonstrate larger changes.

4.2.2 The 'Carbonate' Pathway

The carbonate pathway is shown in Figure 4.4, starting from the excimer species. This pathway has been studied in some detail in the literature, but never in a complete manner. Typical analysis consists of investigation from the formed CO$_2$ linked dimer, through the release of CO, terminating at the bicarbonate linked dimer. Studies typically build the dimer as a three-body reaction, or start with a Re$-$Re bound catalyst dimer and the insertion of CO$_2$. They do not discuss the decomposition to the catalyst ground states, nor the formation in simplest steps.

Energies of each of the compounds involved in this mechanism pathway are shown in Table 4.3, along with the energy of solvation. The full list of reaction energies are listed in Table 4.4.

The mechanism starts with the addition of a CO$_2$ molecule to the excimer, forming
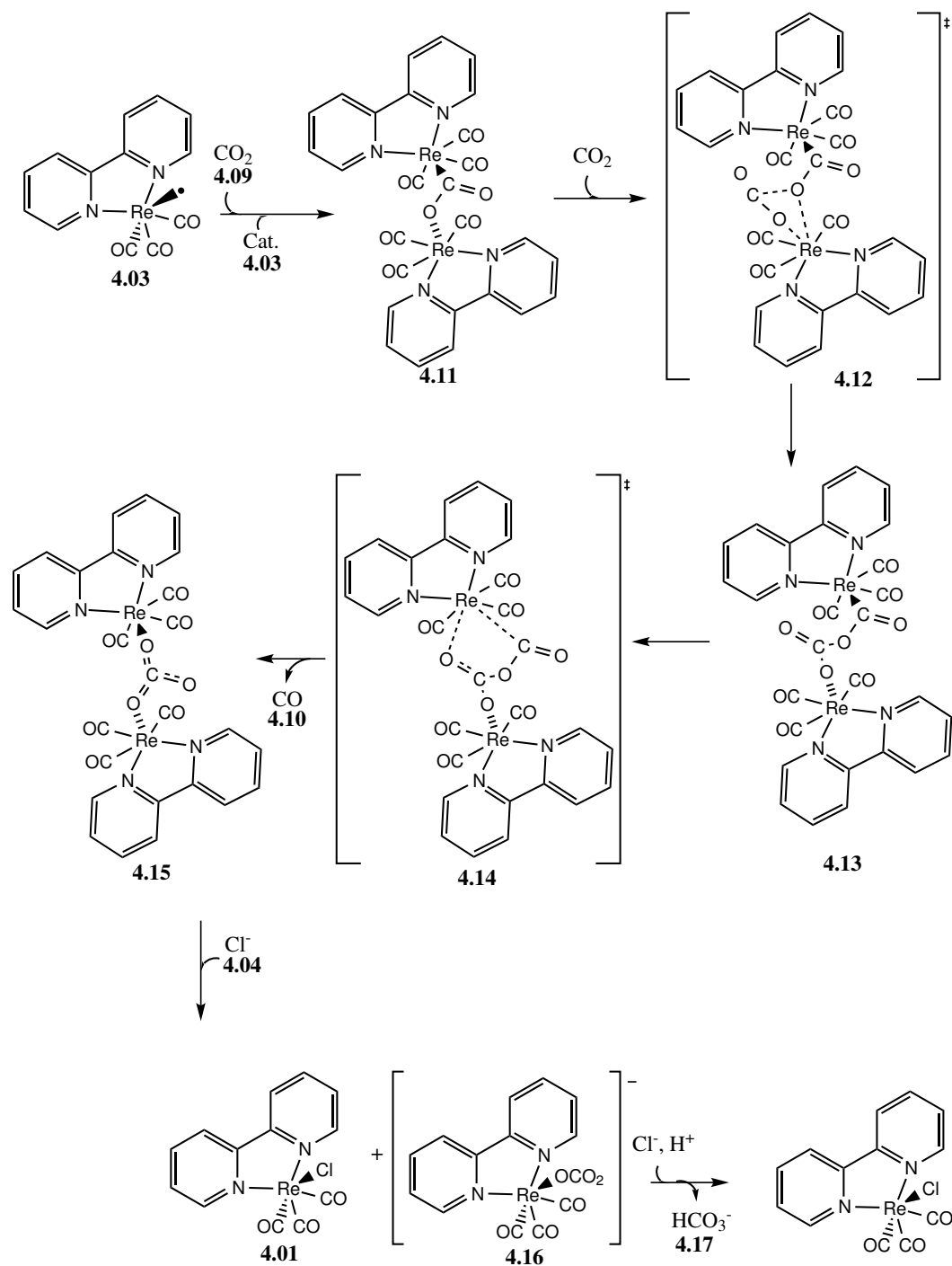
Figure 4.4 The 'carbonate' mechanistic pathway

Table 4.3 Gas phase and solvated energies of compounds, transition states and intermediates in the 'carbonate' mechanism

Label	E (gas)[a]	E (solution)[b]	E (solvation)[c]
4.01	-1374.621419	-1374.651099	18.62
4.03	-914.3139376	-914.3287245	9.28
4.04	-460.2890817	-460.4058583	73.28
4.07	-291.9173706	-291.9211226	2.35
4.09	-188.6945676	-188.6974631	1.82
4.10	-113.3744946	-113.3754466	0.60
4.11	-2017.373132	-2017.412314	24.59
4.12	c	c	#VALUE!
4.13	-2206.047558	-2206.097328	31.23
4.14	c	-2206.061531	#VALUE!
4.15	-2092.678255	-2092.725669	29.75
4.16	-1178.065153	-1178.119717	34.24
4.17	-264.4852375	-264.4967144	7.20
4.18	c	-2017.411256	#VALUE!
4.19	-263.7946209	-264.1983931	253.37
4.27	-914.1064097	-914.1872844	50.75

[a] TPSS SCF energy in hartrees.
[b] TPSS SCF energy in hartrees with COSMO solvation in DMF.
[c] TPSS solvation energy in kcal/mol (E(gas) - E(solution)).

4.11. This is a very weakly bound species when solved in a simulated DMF environment; in the gas phase this transition complex will not solve. The DMF solved structure has a Re-C bond length of 2.50654 Å, and O-C-O bonding angle of 142°, when compared to the Re−C distances of rhenium carbonyls of *ca.* 1.9 Å, this is a very weak bond. The formation of this 'bond' requires only 6.37 kcal/mol, the radical species is not satisfied with the addition of CO$_2$ and requires further electron contribution to become more stable. This unstable complex is able to extract a hydrogen to continue with the formate pathway (see below subsection 4.2.3), or combine with a second molecule of the excimer to form a dimer **4.13**. This dimer formation is explicitly not favoured; although resolution of

Table 4.4 Energies for the reaction steps in the 'formate' pathway

Description		Steps	Energy(gas)[a]	Energy(dmf)[b]
Formation of Radical Anion	4.01, 4.05 $\longrightarrow$ 4.02, 4.06		124.261582	47.596907
Open site catalyst plus cl-	4.02 $\longrightarrow$ 4.03, 4.04		50.816912	15.440887
Reconfiguration of TEA	4.06, 4.05 $\longrightarrow$ 4.07, 4.08		-1.077024	-2.915901
Addition of CO2 to open site		4.4	-0.2501423	6.37310903
addition of second cat to CO2		4.5	118379.026	118375.044
Insertion of CO2		4.6	#VALUE!	-8.5491267
relaxation of co2 insertion		4.7	#VALUE!	-0.6637971
rearrange to 4ring dimer		4.8	#VALUE!	#VALUE!
relax to long		4.9	#VALUE!	#VALUE!
rearrangement to 5ring dimer		4.1	#VALUE!	22.4628711
relax to final		4.11	#VALUE!	-24.839557
break apart		4.12	317.951051	262.714812
return to ground states		4.13	-613.91666	-426.82371

[a] TPSS SCF energy in kcal/mol.
[b] TPSS SCF energy in kcal/mol with COSMO solvation in DMF.

radical species is provided, the transformation via **4.12** is still kcal/mol uphill in DMF. Explanation of this untenably large value may be the root of the choice in literature to utilize the Re-Re bound dimer species as the catalyst starting point, instead of the ground state. The quenching of the radical forms much stronger bonds between the metal atoms and the linking CO$_2$. The Re-C distance has shortened from the 2.50654 Å seen in **4.11** to 2.25829 Å. This is still longer than the Re-CO bonds, expected due to the lack of π back-bonding observed with carbonyl ligands, however, it corresponds with similar published crystal structures of Re-C bond lenghts for sp^2 carbons.[109] The Re-O bond is 2.13 Å, a value that remains constant for Re-O through the intermediates in the reaction pathway.

After the dimer **4.13** has been formed, a second molecule of CO$_2$ is inserted via **4.14** to form the Re-C-O-C-O-Re complex **4.15**. This linker contains bonds from length 1.28 - 1.44 Å, typical for sp^2-carbon oxygen bonds. Bond angles are typically just under

numb

From this point onwards the reaction proceeds in achievable downhill steps, the formation of the dimer is the rate limiting step for the en-

the idealized 120° expected as well. Due to the linker, the catalyst ligand bipyridines have moved from a nearly co-planar geometry to a nearly perpendicular geometry. Re-C and Re-O bonds remain constant in length compared to **4.13**. Following the insertion of a second molecule of CO$_2$, internal rearrangements progress this complex through the release of a molecule of CO and the formation of the bicarbonate byproduct. The formation of a 5 membered ring in the **4.16** transition state leads to the release of the CO and the formation of a carbonate linked dimer, **4.17**. The carbonate dimer species is left to decompose to a catalyst cation **4.20** with an open site, and the bicarbonate adduct **4.18**. This carbonate dianion may pick up a proton before or after the disassociation to the catalyst cationic species, resulting in the released of the bicarbonate species to solution (**4.19)** when the catalyst is returned to ground state **4.01** with addition of a chloride

ref

Some work done by Agarwal *et. al.*provides an opportunity for a catalytic pathway with similar results requiring only one molecule of catalyst. Instead of capping the loosely coordinated CO$_2$ with the eximer, the radical is quenched with a hydride extraction from the sacrificial amine, much as in the pathway described in subsection 4.2.3. A second molecule of CO$_2$ reacts with the acid, undergoing a series of steps to produce the carbonate. The experimental data supporting this variation of the mechanism is not strong, further validation should be required for this variation to gain traction in the literature.

4.2.3   The 'Formate' Pathway

In comparison to the catalytic dimer formed in the carbonate pathway above, the formate formation occurs via a much simpler mechanism. The addition of a proton to the open site axial to the ligand occurs via the simultaneous electron and proton transfer from

a by-product of the reduction of the amine. CO$_2$ inserts into this metal hydride bond, resulting in a metal-oxide bond, with the formate anion. Separation of the weak metal-oxygen bond allows for the reinsertion of the halide to the cationic metal centre.
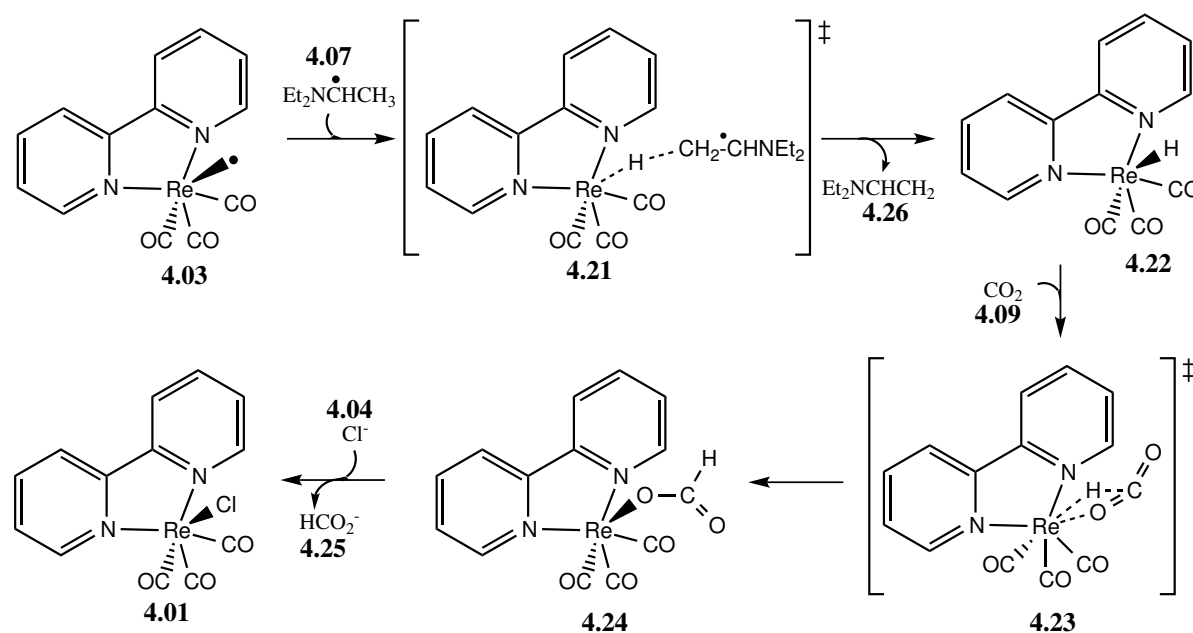
Figure 4.5 The 'formate' mechanistic pathway

Energies of each of the compounds involved in this mechanism pathway are shown in Table 4.5, along with the energy of solvation.

After formation of the excimer **4.03**, the radical species extracts a hydrogen atom from the oxidized chain of the sacrificial amine **4.07**, a step with a barrier of -9.83kcal/mol in DMF. The sacrificial amine involved in this step had previously had one proton extracted by another molecule of the amine in a proton exchange step (see subsection 4.2.1), resulting in a neutral radical. Extraction of the proton and electron pair allows for the formation of an ethene arm, completing the decomposition of the amine to the final neutral, singlet molecule **4.26**. Relaxation of this transition state results in the hydrogen extraction from the radical species, yielding the formation of the hydride complex **4.22**.

Table 4.5 Gas phase and solvated energies of compounds, transition states and intermediates in the 'formate' mechanism

Label	E (gas)[a]	E (solution)[b]	E (solvation)[c]
4.01	-1374.621419	-1374.651099	18.62
4.03	-914.3139376	-914.3287245	9.28
4.04	-460.2890817	-460.4058583	73.28
4.07	-291.9173706	-291.9211226	2.35
4.09	-188.6945676	-188.6974631	1.82
4.10	-113.3744946	-113.3754466	0.60
4.21	-1206.224778	-1206.265516	25.56
4.22	-914.9204746	-914.9448354	15.29
4.23	-1103.581201	-1103.619960	24.32
4.24	-1103.635283	-1103.665628	19.04
4.25	-189.3051464	-189.4151284	69.01
4.26	-291.3467768	-291.3525868	3.64
4.27	-914.1064097	-914.1872844	50.75

[a] TPSS SCF energy in hartrees.
[b] TPSS SCF energy in hartrees with COSMO solvation in DMF.
[c] TPSS solvation energy in kcal/mol (E(gas) - E(solution)).

Table 4.6 Energies for the reaction steps in the 'formate' pathway

Description		Steps	Energy(gas)[a]	Energy(dmf)[b]
Formation of Radical Anion	4.01, 4.05 $\longrightarrow$ 4.02, 4.06		124.261582	47.596907
Open site catalyst plus cl-	4.02 $\longrightarrow$ 4.03, 4.04		50.816912	15.440887
Reconfiguration of TEA	4.06, 4.05 $\longrightarrow$ 4.07, 4.08		-1.077024	-2.915901
Hydride Extraction		1.4	4.09794743	-9.8319638
Removal of TEA		1.5	-26.652434	-20.021496
Insertion of CO2		1.6	21.2356096	14.0177223
recoordination		1.7	-33.936535	-28.657394
dissasotiation of HCO2-		1.8	140.389052	39.6680755
Reformation of Catalyst		1.9	-141.76995	-36.367745

[a] TPSS SCF energy in kcal/mol.
[b] TPSS SCF energy in kcal/mol with COSMO solvation in DMF.

This hydride complex is able to insert a molecule of CO$_2$ into the metal-hydrogen bond, in transition step **4.23**. While typically seen in other organo-metal chemistries, rhenium(I) hydrides are very rare, only appearing as intermediates in these mechanisms. The Re-H bond length is Å, compared to the length of the Re-Cl bond from the ground state **4.01** species. When a molecule of CO$_2$ approaches, the transition state of a pseudo-septa-coordinate species forms. The formation is expensive, at just over 14 kcal/mol. The Re-H bond increases in length to Å, the Re-O bond is Å, and the O-Re-H angle remains tight at °. This step completes with 28.66 kcal/mol energy release to form the formato anion complex **4.24**.

The formato anion **4.25** dissociates with a chloride re-entry requiring less than 3 kcal/mol for the dissociation. This counterion exchange is likely more favoured in the real solution, not all contributions from products and the electrolyte are included in the calculation. Further reactions of the formato anion in solution are not investigated, but the anion likely remains deprotonated in the slightly basic environment.

4.2.4 The 'Water-Gas Shift' Pathway

The water-gas shift mechanism involves the addition of two protons from the reductant to a CO$_2$ molecule bound to the metal centre. The first proton addition yields an acid species, this is dehydrated via the second addition of a proton and the release of one molecule of H$_2$O. The resulting tetracarbonyl cationic species is able then to release an axial carbonyl to return to the ground state. While any of the carbonyl groups could be labile, the carbonyl at the axial position is the one actively replaced by the halide to return to the starting catalyst.[110]

Energies of each of the compounds involved in this mechanism pathway are shown in Table 4.7, along with the energy of solvation.
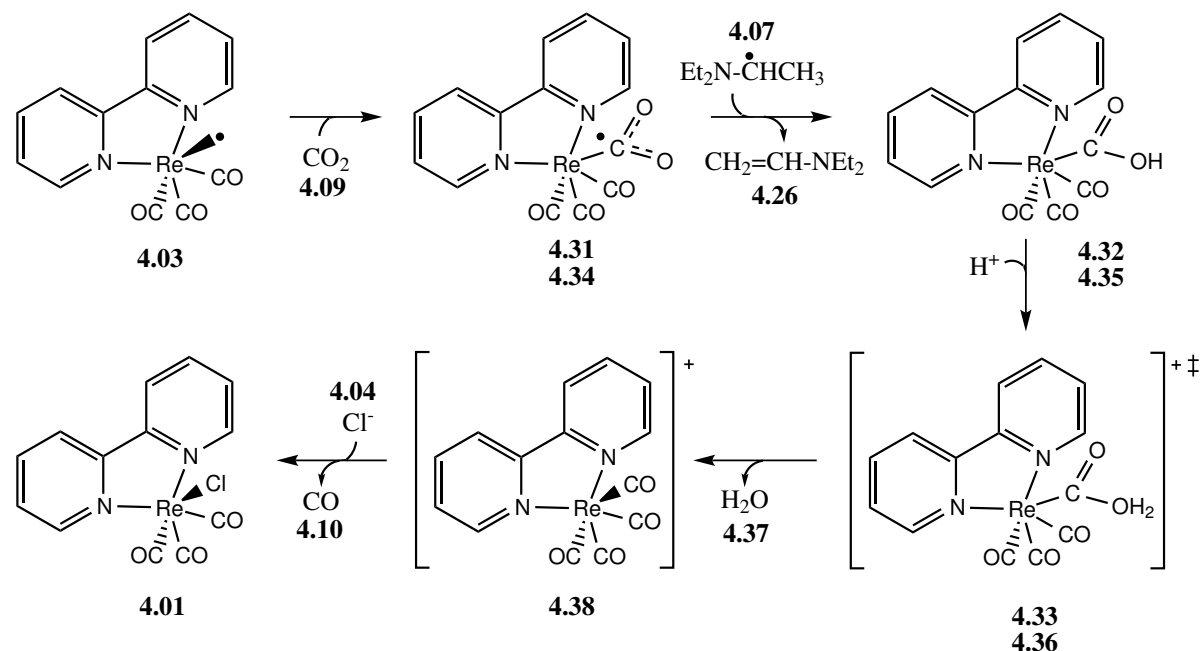
Figure 4.6 The 'water-gas shift' mechanistic pathway

This mechanistic pathway it thought to start by the same addition of CO2 that is seen in the carbonate mechanism (see subsection 4.2.2, forming **4.31**. The added CO_2 is able to extract a hydrogen from the once-reduced sacrificial amine **4.07**, allowing the completion of the ethene formation **4.26**. The newly formed acid species **4.32** dehydrates in the presence of a second proton (via **4.33**) to form water **4.37** and the tetracarbonyl cationic species **4.38**.

Typically, this reaction had been thought to proceed on the axial site of the catalyst, mirroring the pathways discussed above. However, due to the ease of migration of the carbonyl groups, it is proposed that the 'water-gas shift' mechanism does not occur entirely axial to the ligand, but begins with coordination of a CO_2 molecule in between the *facial*-CO ligands, forcing a carbonyl to the axial position **4.34**. This CO_2 bound in the plane of the ligand then undergoes hydrogen addition and dehydration to produce a molecule of H_2O, continuing as before. While any of the carbonyl groups could be labile,

Table 4.7 Gas phase and solvated energies of compounds, transition states and intermediates in the 'water-gas shift' mechanism

Label	E (gas)[a]	E (solution)[b]	E (solvation)[c]
4.01	-1374.621419	-1374.651099	18.62
4.03	-914.3139376	-914.3287245	9.28
4.04	-460.2890817	-460.4058583	73.28
4.07	-291.9173706	-291.9211226	2.35
4.10	-113.3744946	-113.3754466	0.60
4.26	-291.3467768	-291.3525868	3.64
4.31	-1103.008904	-1103.016031	4.47
4.32	-1103.610331	-1103.640451	18.90
4.33	-1104.018352	-1104.093194	46.96
4.34	-1102.963633	-1102.992198	17.92
4.35	-1103.597572	-1103.625739	17.68
4.36	-1104.016748	-1104.092840	47.75
4.37	-76.46413339	-76.47581393	7.33
4.38	-1027.546073	-1027.619412	46.02
4.39	-1394.956766	-1394.991144	21.57
4.40	-1394.979805	-1394.970048	-6.12
4.41	-914.2766988	-914.2972247	12.88

[a] TPSS SCF energy in hartrees.
[b] TPSS SCF energy in hartrees with COSMO solvation in DMF.
[c] TPSS solvation energy in kcal/mol (E(gas) - E(solution)).

the carbonyl at the axial position is replaced by the halide to return to the starting catalyst.[110]

Table 4.8 Energies for the reaction steps in the 'formate' pathway

Description	Steps		Energy(gas)[a]	Energy(dmf)[b]
Formation of Radical Anion	4.01, 4.05 $\longrightarrow$	4.02, 4.06	124.261582	47.596907
Open site catalyst plus cl-	4.02 $\longrightarrow$	4.03, 4.04	50.816912	15.440887
Reconfiguration of TEA	4.06, 4.05 $\longrightarrow$	4.07, 4.08	-1.077024	-2.915901
migration of open site?		2.4	23.3674263	19.7662463
Addition of CO2 to open site		2.5	4.78987184	1.56207334
H transfer to CO2		2.6	-61.998066	-35.596525
CO2H planar relaxation		2.7	22.2489536	-5.1943905
COOH2 ts		2.8	144.908364	116.570584
CO4 + and water		2.9	4.10436095	-1.4970678
dissassotiation of CO		2.10	40.893777	35.5673996
Reformation of Catalyst		2.11	-141.76995	-36.367745

[a] TPSS SCF energy in kcal/mol.
[b] TPSS SCF energy in kcal/mol with COSMO solvation in DMF.

4.2.5 Consequences From κ^2 Terpyridine Complex Inactivity

The lack of reactivity of the κ^2(terpy)Re(CO)$_3$X motif of complexes contrasting to the activity of the originally published κ^2(bipy)Re(CO)$_3$X indicates some influence of the ligand on the mechanism. While the terdentate complex can be rationalized to be inactive due to its short-lived excited state (as seen in the lack of fluorescence), this explanation does not suffice for the fluorescing bidentate complex. Other substituted bipyridine ligands are known to be active for photocatalytic reduction, identifying the most likely conflicting feature of the terpyridine ligand to be the pendant arm, and its availability for chelation to the metal centre. While in the radical eximer form, the chelation site is sterically blocked by one of the three carbonyl groups. However, reorganization of the substituent carbonyls from a *facial* orientation to a *meridional* could allow for the free pyridine to form the metal-ligand bond, resulting in compound (X)

fluorescence
tests on 1,2

ref lehn88?

Table 4.9 Energies for the reaction steps in the 'formate' pathway

Description	Steps	Energy(gas)[a]	Energy(dmf)[b]
Formation of Radical Anion	4.01, 4.05 $\longrightarrow$ 4.02, 4.06	124.261582	47.596907
Open site catalyst plus cl-	4.02 $\longrightarrow$ 4.03, 4.04	50.816912	15.440887
Reconfiguration of TEA	4.06, 4.05 $\longrightarrow$ 4.07, 4.08	-1.077024	-2.915901
Addition of CO2 to open site	3.4	-0.2501423	6.37310903
H transfer to CO2	3.5	-19.133571	-33.878805
CO2H axial relaxation	3.6	-0.2145456	-1.1883574
COOH2 ts	3.7	151.907871	125.579781
CO4 + and water	3.8	5.1112987	-1.2748062
dissassotiation of CO	3.9	40.893777	35.5673996
Reformation of Catalyst	3.10	-141.76995	-36.367745

[a] TPSS SCF energy in kcal/mol.
[b] TPSS SCF energy in kcal/mol with COSMO solvation in DMF.

4.3   Comparison Between Mechanistic Pathways

Previous studies in literature had only analyzed one possible mechanistic pathway (or a subsection thereof), without a fuller analysis of the competitiveness of each pathway relative to the others. Discussion on the tenability of each potential pathway relied on the *in situ* observation of intermediates or transition states, the success (or lack thereof) of synthesis of the intermediates, and the relative production of by-products in the mechanistic trials.

The overall energies for each of the mechanistic pathways shown in Figure 4.1 are shown in Figure 4.7.

Figure 4.7 An overview of the energies of the three mechanistic pathways of photochemical CO$_2$ reduction

SOLVE EN-
ERGY

4.4 Conclusions

With the energies of each of the independent mechanisms elucidated, the feasibility of each mechanism becomes evident. Evidence in literature suggests that all mechanisms progress to some degree, however, the production of CO outpaces that of the partial reduction or oxidation pathways.

Chapter 5

TurboControl

The analysis of the mechanism using computational methods required a significant amount of manual set-up and analysis work of computational input and output files. The calculations required 38 different molecules, intermediates, or transition states to be calculated in multiple different environments. These calculations typically require intervention or set-up of intermediate steps to be able to fully elucidate all of the required information, for example, the set-up of frequency calculations after a geometry optimization to ensure ground state or transition state geometries.

Additionally, while TurboMole contains much faster optimization code for DFT calculations, the user interface for this software requires a significant learning curve and is based in a user-abrasive interactive text prompt environment. This contrasts to Gaussian 09, which is significantly more popular, partially due to the user-friendliness of the GaussView Graphical User Interface (GUI), despite concerns about the speed of optimization of large or complex molecules.

These two factors prompted the development of a new program, TurboControl, written in Python, with the goal of combining the user friendliness of GaussView on top of the optimization efficiency of TurboMole. This program allows a user to prepare the input

files in GaussView, modify them slightly in any text editor available to them, then run a batch calculation on the files. TurboControl monitors the computational jobs, resubmitting for frequency calculations when optimization is complete if requested, and using the TurboMole tools available when required to ensure ground state or first transition state geometries are discovered. TurboControl then outputs statistics files, providing the energy and first frequency vibration of each molecule in a single output file. Additional commands can instruct TurboControl to run in a solution, do single-point energy calculations, or gather more in-depth thermodynamic information from the outputs using TurboMole's tools.

TurboControl provides this hands-off management of jobs allowing the user to spend more time in data analysis, experimental work, or to be able to produce data at a significantly higher rate compared to the manual setup and monitoring of jobs. TurboControl also contains a single job initiation script entitled TurboGo to allow for the use of the input files without the overhead of the job managing.

5.1   Development

TurboControl began as a script for the simple setup and submission of jobs in TurboMole from Gaussian input files. The jobs were submitted to the 'wooki' computing cluster available at the University of Ottawa. This computing cluster consists of approximately 1000 CPU cores, running the CentOS distribution of Linux available in the Rocks software distribution. The GridEngine queuing system ensures fair usage of computing cores for each user, and maximizes throughput by managing computational jobs.

TurboControl initially submitted jobs and monitored their successful completion or failure. Development quickly expanded to include automatic resubmission for frequency analysis of geometry optimization jobs, required to determine the success of finding an

energy minima (stationary point) instead of a transition state. As the complexity of the mechanistic study (see chapter 4) increased to include analysis of thermodynamic data, calculation of transition states, calculation in solution phases, and more, the capabilities of TurboControl increased to meed these demands.

Turbocontrol is now able to handle large batches of input, with jobs of varying complexity and monitor them through successful completion or failure of TurboMole. Analysis of the computational jobs is performed to simply highlight DFT energies, first computed normal mode frequencies, and thermodynamic properties (if requested).

5.2   Usage

TurboControl is available freely on the internet, and is a fully open-source project.[111] The code may be downloaded by anyone and used without prior permission for personal, academic, or commercial purposes, provided that the original software license remains with the code. TurboControl works only with the stated versions of software in the 'readme' file available with the code on the internet (and included in Appendix C). The software requires no installation prior to use, and has very few dependencies beyond the typically installed packages on a unix or linux system.

TurboControl and TurboGo are not quantum mechanical packages themselves, they require a properly licensed installation of TurboMole to perform calculations. Additionally, while GaussView may be used to prepare the input files, modification of the files by hand in a text editor is required to access most features, GaussView is not required for the use of TurboControl.

Chapter 6

Conclusions

The target Re^{I} terdentate terpyridine compounds were successfully synthesized, characterized, and tested for photocatalytic CO_2 reduction. The catalysts show no activity for the reduction, in contrast to the known excellent bipyridine compounds.

The reaction mechanisms were studied successfully with DFT methods, resulting in the proposed new geometry for the production of CO with no carbonate or formate anions. This new geometry does not conflict with known experimental studies, yet avoids three-body mechanistic steps.

Appendix A

Experimental Procedures

Experimental synthesis and characterization data for the compounds discussed in this thesis are shown below by compound number:

A.1   General Methods

Synthesis reactions were set-up in a glovebox under a nitrogen atmosphere and performed under an inert atmosphere. Solvents were sparged with nitrogen and then dried by passage through a column of activated alumina using an apparatus purchased from Anhydrous Engineering. Deuterated chloroform and deuterated acetonitrile was dried using activated molecular sieves. Rhenium starting materials were purchased from Strem Chemicals and used as received. All other chemicals were purchased from Aldrich and used without further purification. NMR spectra were run on Bruker Avance 400MHz spectrometers with CD_3CN or $CDCl_3$ as solvent and internal standard. Elemental analyses were performed by Midwest Microlab LLC, Indianapolis IN. Solid state reactions were carried out in a Lindberg Blue M Mini-Mite Tube Furnace (model TF55035A-1). Infrared spectra were collected using an Agilent Technologies Cary FT-IR spectrome-

ter using a diamond ATR attachment. UV-Vis spectra were collected using a Agilent Technologies Cary 5000 UV-Vis spectrometer. TGA was performed on a TA Q5000 IR instrument: approximately 10-15 mg of each sample was placed in a ceramic sample pan which was heated at a rate of 5°C/min up to 150°CC, followed by a rate of 2°CC/min to 300°C while being purged with N_2 at a flow rate of 25 mL/min. GC was performed using a HP gas chromatograph with a 15 m CARBONPLOT column with 0.320 mm inner diameter and 1.50 μm film in a 40°C oven. The instrument is fitted with a TCD at 220°C.

A.2   Computational Methods

For the UV-Vis and experimental correlation study, the structures of all species were optimized using Gaussian 09[72] employing the B3LYP[73,74] exchange-correlation (XC) functional. The LanL2DZ basis set/effective core potential[75] was used on Re and, the all-electron TZVP basis set[76] for the remaining lighter atoms. Frequency analysis of all structures was used to confirm the nature of the stationary points. Solvent effects were computed using the integral equation formalism variant of the PCM solvation model within Gaussian 09 for both the ground state and excited state TD-DFT calculations with DMSO as the solvent.[77,78] The UV-Vis absorption spectra were extracted using the Chemissian software.[112] In these calculations, a pseudo-Voigt band shape was employed with a default average band width at half-height of 2000cm^{-1}.

For the mechanism study, the ground and transition state structures and energies of all species were obtained by using TurboMole 6.5 software[88,89] with the TPSS meta-GGA XC functional.[90] The def2-TZVP basis set was used for all atoms.[76,91] The TurboMole program contains a number of optimizations to the original DFT algorithms,[92–100] decreasing the calculation time without compromising accuracy. Grimme's dispersion cor-

rection (version 3) was included in the calculations.[101] Intermediates and transition states were verified by frequency analysis.[97,102,103] The effects of solvation was calculated using the Conductor-like Screening Model (COSMO) implemented in TurboMole,[104] which is a continuum solvation model implicitly surrounding the solute molecule.

A.3 X-ray Crystallography

Crystals were mounted on thin glass fibers using paraffin oil. Prior to data collection crystals were cooled to 200.15K. Data were collected on a Bruker AXS SMART single crystal diffractometer equipped with a sealed Mo tube source (wavelength 0.71073 Å) APEX II CCD detector. Raw data collection and processing were performed with APEX II software package from BRUKER AXS53. Diffraction data for sample **3** was collected with a sequence of 0.5° ω scans at 0, 120, and 240° in ϕ. Due to lower unit cell symmetry in order to ensure adequate data redundancy, diffraction data for **1**, **2** and **8** were collected with a sequence of 0.5° ω scans at 0, 90, 180 and 270° in ϕ. Initial unit cell parameters were determined from 60 data frames with 0.3° ω scan each collected at the different sections of the Ewald sphere. Semi-empirical absorption corrections based on equivalent reflections were applied.[113] Systematic absences in the diffraction data-set and unit-cell parameters were consistent with triclinic P$\bar{1}$ ($\mathcal{N}^{\mathcal{O}}2$) for compounds **1**, **2** and **8**, monoclinic **C**2/c ($\mathcal{N}^{\mathcal{O}}15$) for compound **3**. Solutions in the centrosymmetric space groups for all compounds yielded chemically reasonable and computationally stable results of refinement. The structures were solved by direct methods, completed with difference Fourier synthesis, and refined with full-matrix least-squares procedures based on F^2.

Solutions for **1** and **2** revealed that both these structures contain two compound molecules per asymmetric unit.

Initial refinement results for the compound **1** suggested presence of two non-merohedrally twinned domains. Two independent orientation matrices were found using CELL_NOW software.[114] Data set was re-integrated with two independent orientation matrices and consecutive model refinement was performed using HKLF5 format reflection data file. Twinning domain ratio coefficient (BASF) was successfully refined to 0.3794.

On the final model refinement stage for compound **2** thermal motion parameters for coordinated CO (-C(33)=O(3)) and Cl (Cl(2)) moieties as well as presence of unusually strong residual electron density peaks in one of the compound molecules suggested a positional CO / Cl disorder not related by symmetry. Disorder was successfully modeled with refined occupation ratio at one position CO / Cl = 70%:30%. Disorder of the second position was inversed in such way that overall occupancy summed up to one full CO and one full Cl ligands in the first coordination sphere of Re metal center. Set of geometrical (SADI) and thermal motion (SIMU, DELU) restrains were applied to achieve acceptable molecular fragment geometries and thermal motion parameter values.

For all the compounds hydrogen atoms positions were initially assigned from the residual electron density peaks coordinates. However, after initial placement all hydrogen atoms were treated as idealized contributions during the refinement. All scattering factors are contained in several versions of the SHELXTL program library, with the latest version used being v.6.12.[115]

A.3.1   X-Ray Structures from Multiple Vantage Points

Multiple views of each x-ray structure discussed in chapter 2.

A.4   (terpy-κ^2-N,N$'$)Re(CO)$_3$Cl (1)

Re(CO)$_5$Cl (201 mg, 0.556 mmol) and 2,2:6,2 terpyridine (129 mg, 0.553 mmol) were mixed in 60 mL of toluene. The reaction mixture was heated to 100C for 1 hour under N2. During this time the solution turned a bright red. Upon cooling a yellow precipitate was formed. The solution was filtered, and the solid was washed with diethyl ether, and dried under vacuum. Compound **1** is a bright yellow powder that was isolated in 70 % yield (208 mg). Crystals were obtained from chloroform with addition of a small amount of hexanes as counter solvent. TGA: 8 % mass loss from 240-280°C. FTIR: 2019, 1981, 1889 cm^{-1} (v C=O). ^{1}H NMR (CD$_3$CN, 400 MHz): δ 9.06 (ddd, J=5.6, 1.7, 0.8 Hz, 1H), 8.77 (ddd, J=4.9 Hz, 1H), 8.49 (td, J=8.2, 1.5 Hz, 2H), 8.28 (t, J=7.9 Hz, 1H), 8.22 (td, J=8.1, 1.6 Hz, 1H), 7.96 (td, J=7.8, 1.8 Hz, 1H), 7.79 (dt, J=7.8, 1.1 Hz, 1H), 7.80 (dd, J=7.7, 1.0 Hz, 1H), 7.63 (ddd, J=7.6, 5.5, 1.2 Hz, 1H), 7.55 (ddd, J=7.6, 5.0, 1.0 Hz, 1H). Elemental analysis calculated (%) for [C$_{18}$H$_{11}$ReClN$_3$O$_3$]: C 40.11, H 2.06, N 7.80, found C 39.96, H 2.09, N 7.69.

A.5   (terpy-κ^3-N,N$'$,N$'$ $'$)Re(CO)$_2$Cl (2)

Compound **1** (101 mg, 0.187 mmol) was placed in a tube furnace and heated to 240^circC under N$_2$ flow for 60 minutes. A black solid was collected (90 mg) at 94 % yield based on the formula for **2**. Crystals were obtained from chloroform with addition of a small amount of hexanes as counter solvent. FTIR: 1872, 1788 cm^{-1} (v C=O). ^{1}H NMR (CD$_3$CN, 400 MHz): δ 8.70 (ddd, J=4.7, 1.8, 0.9 Hz, 2H), 8.65 (dt, J=8.0, 1.0, 1.0, 2H), 8.47 (d, J=7.8 Hz, 2H), 8.03 (t, J=7.8 Hz, 1H), 7.95 (td, J=7.7, 7.7, 1.9 Hz, 2H), 7.43 (ddd, J=7.5, 4.8, 1.2 Hz, 2H). Elemental analysis calculated (%) for [C$_{17}$H$_{11}$ReClN$_3$O$_2$]: C 39.96, H 2.17, N 8.22, found C 39.62, H 2.09, N 7.99.

A.6 (terpy-κ^2-N,N′)Re(CO)$_3$Br (3)

Re(CO)$_5$Br (191 mg, 470 mmol) and 2,2:62 terpyridine (129 mg, 0.553 mmol) were allowed to react under conditions analogous to the preparation of **1**. A bright yellow powder was obtained, 0.223 g (0.382 mmol, 81 %). FTIR: 2012, 1910, 1886 cm^{-1} (v C=O). ^{1}H NMR (CD$_3$CN, 400 MHz): δ 9.07 (ddd, J=5.6, 1.6, 0.9 Hz, 1H), 8.77 (ddd, J=4.6, 1.5, 0.8 Hz, 1H), 8.52 8.48 (m, 2H), 8.28 (t, J=7.9 Hz, 1H), 8.21 (td, J=8.0, 1.6 Hz, 1H), 7.97 (td, J=7.8, 1.8 Hz, 1H), 7.80 7.75(m, 2H), 7.63 (ddd, J=7.6, 5.5, 1.2 Hz, 1H), 7.55 (ddd, J=7.7, 4.9, 1.1 Hz, 1H). Elemental analysis calculated (%) for [C$_{18}$H$_{11}$ReBrN$_3$O$_3$]: C 37.06, H 1.90, N 7.20, found C 36.94, H 1.92, N 7.00.

A.7 (terpy-κ^3-N,N′,N″)Re(CO)$_2$Br (4)

Compound **3** (182 mg, 0.312 mmol) was placed in an tube furnace and heated to 230°C under N$_2$ flow for 60 minutes. A black solid was collected, 0.155 mg (0.279 mmol, 89 % yield). Crystals were obtained from chloroform with addition of a small amount of hexanes as counter solvent. FTIR: 1873, 1794 cm^{-1} (v C=O). ^{1}H NMR (CD$_3$CN, 400 MHz): δ 8.95 (d, J=5.4 Hz, 2H), 8.24 (t, J = 8.1Hz, 4H), 8.05 (dd, J=8.2, 7.7 Hz, 1H), 7.90(td, J=7.9, 1.7 Hz, 2H), 7.63 (ddd, J=7.3, 5.5, 1.2 Hz, 2H) Elemental analysis calculated (%) for [C$_{17}$H$_{11}$ReBrN$_3$O$_2$]: C 36.76, H 2.00, N 7.57, found C 36.66, H 2.00, N 7.50.

A.8 (terpy-κ^2-N,N′)Re(CO)$_3$OTf (7)

To **1** (80 mg, 0.148 mmol), AgCF$_3$SO$_3$ (46 mg, 0.179 mmol) was added in 10 mL CH$_3$CN. The reaction was stirred 24 h and kept dark. Solution was filtered to remove salts, then

reduced in volume. Cold diethyl ether was used to precipitate product. Yellow-grey powder (**7a**) was collected by filtration, yielding 38mg (40 %). Crystals were grown from saturated chloroform with hexanes as countersolvent for X-ray crystallography. FTIR: 2030, 1895, 1890 cm^{-1} (v C=O), 1280, 1228, 1204 cm^{-1} (v SO$_3$). ^{1}H NMR (CD$_3$CN, 400 MHz): δ 9.05 (ddd, J=5.5, 1.6, 0.8 Hz, 1H), 8.79 (ddd, J=4.9, 1.8, 1.1 Hz, 1H), 8.57 (dd, J=8.1, 0.9 Hz, 1H), 8.54 (dt, J=8.2, 1.1 Hz, 1H), 8.37 (t, J=7.9 Hz, 1H), 8.31 (td, J=8.0, 1.6 Hz, 1H), 8.03 (td, J=7.7, 1.7 Hz, 1H), 7.87 (dd, J=7.8, 1.0 Hz, 1H), 7.75 (dt, J=7.8, 1.1 Hz, 1H), 7.72 (ddd, J=7.4, 5.9, 1.1 Hz, 1H), 7.61 (ddt, J=7.7, 4.8, 0.5, 0.5 Hz, 1H). Elemental analysis calculated (%) for [C$_{19}$H$_{11}$ReN$_3$O$_6$F$_3$S]: C 34.97, H 1.70, N 6.44, found C 31.80, H 1.73, N 5.33.

Alternately, to **1** (72 mg, 0.134 mmol) was added 10 mL CF$_3$SO$_3$H (excess) and temperature was increased to for 20 minutes. A black solution was neutralized with addition of 5% Na$_2$CO$_3$ in H$_2$O. Product was extracted with CHCl$_3$, then dried under vacuum to yield a brown solid (**7b**) (47 mg, 54 %).

A.9   (terpy-κ^3-N,N′,N″)Re(CO)$_2$OTf (8)

To **2** (77 mg, 0.143 mmol), AgSO$_3$CF$_3$ (47 mg, 0.183 mmol) was added in 15 mL CH$_3$CN. Solution was refluxed for 6 h in the dark under N$_2$ atmosphere. Solution was filtered, then reduced to minimal volume. Cold diethyl ether was added dropwise to precipitate product. Collected by filtration and washed with additional cold ether, yielding 75 mg (120 mmol, 80 %). Crystals grown from saturated methylene chloride, with hexanes as countersolvent for x-ray crystallography. FTIR: 1910, 1829 cm^{-1} (v C=O), 1259, 1224, 1143 cm^{-1} (v SO$_3$). ^{1}H NMR (CD$_3$CN, 400 MHz): δ 8.91(ddd, J=5.6, 1.6, 0.7 Hz, 2H), 8.32 (d, J=8.0 Hz, 2H), 8.28 (ddd, J=8.1, 1.4, 0.8 Hz, 2H), 8.19 (dd, J=8.8, 7.4 Hz, 1H), 8.02 (td, J=7.9, 1.5 Hz, 2H) 7.46 (ddd J=7.6, 5.6, 1.3 Hz, 2H). EA Elemental analysis

calculated (%) for [$C_{18}H_{11}ReF_3SN_3O_5$]: C 34.62, H 1.78, N 6.37, found C 31.02, H 1.82, N 7.11.

Appendix B

Molecular Orbitals and Energy Diagrams

Frontier Molecular Orbitals (MOs) for each compound discussed in this thesis are collected below. These orbitals are generated with the Chemissian program.[112]

Figure B.1 Frontier Molecular Orbitals for **1**

Appendix C

TurboControl and TurboGo Manual

TurboControl is a series of scripts to run Turbomole jobs from Gaussian style inputs. The following is the user manual included with distributions of TurboControl

C.1   Introduction

Gaussian software is well known for the user friendly GUI it contains (via GaussView). Turbomole, another computational suite, is known for its speed and optimizations, but has a significantly higher learning curve and is less beginner friendly. This software is an attempt to be able to use the user friendly input from Gaussian to smooth over the use of Turbomole.

C.2   System Requirements

There are two user-facing scripts available, both written to work with Turbomole 6.1-6.5 on clusters using Grid Engine queuing software. The only tests of operation are on a system with the following details:

- Rocks 6.1 (Emerald Boa)/CentOS 6.3

- Open Grid Scheduler/Grid Engine 2011.11p1

- Python 2.7.3

Other systems, including different operating systems, different versions of Grid Engine or python, or on other systems, are not supported.

Python dependencies include:

- pexpect 3.2[116]

- openbabel[117,118] (optional)

Prior to running TurboGo or TurboControl, a valid installation of Turbomole must be available. On systems where computational modules must be loaded, Turbomole must have been loaded to the environment. Additionally, running the Turbomole environment configuration is recommended but not required prior to launching TurboGo or TurboControl:

```
$ source $TURBODIR/Config_turbo_env
```

C.3   TurboGo

TurboGo is a script fun on an input file. It generates the inputs required for Turbomole jobs, and submits the job to the GridEngine queue before quitting. TurboGo is run with the following syntax:

```
$ turbogo [-h] [-v] [-q] file
```

positional arguments:

```
file                 Read input from gaussian-type input FILE.
```

More info on the input files is available below.

optional arguments:

- `-h, --help` Show this help message and exit

- `-v, --verbose` Run more verbose (show debugging info)

- `-q, --quiet` Run less verbose (show only warnings)

TurboGo saves a log file (turbogo.log) in the directory in which it is run. A second logfile (define.log) will remain if the setup crashes or is terminated at some points, or if the script is run verbose.

TurboGo writes the final coordinates to final_geometry.xyz. If openbabel is installed, it will also write finalgeom.mol. The entire optimization is written to optimization.xyz for viewing with a molecular viewer, such as vmd.

C.4 TurboControl

TurboControl is a management script called from a parent directory containing sub directories of input files. Each input file must be in its own directory. The input file format must be the same as the input format for TurboGo (listed above), with the extension '.in', '.inp', '.input', '.com', or '.gjf'. TurboControl reads the inputs and submits the jobs to the computational cluster queue. It then monitors running jobs to determine when the script has finished. If the job is an Opt-Freq, it prepares the frequency analysis and resubmits to the queue. TurboControl analyzes completed Opt-Freq jobs for true optimization, and attempts to re-run jobs with modified geometries when Transition States are found. TurboControl will not get stuck on the same transition state, but will return a 'stuck' job. TurboControl is run with the following syntax:

```
$ turbocontrol [-h] [-v/-q] [-s]
```

Optional arguments:

- `-h, --help` Show this help message and exit

- `-v, --verbose` Run more verbose (show debugging info)

- `-q, --quiet` Run less verbose (show only warnings)

- `-s, --solvent` List available solvents for COSMO and quit

TurboControl outputs information every 3 hours on the status of the jobs. It writes a logfile (`turbocontrol.log`) and may or may not leave other log files in each directory (depending on verbosity level). Ends when the last job finishes or crashes. Requires 1 node or can be run on headnode (minimal resource consumption especially after initial job preparation and submission.)

TurboControl assists with analysis by outputting a `stats.txt` file as jobs complete. This file contains file details, optimization and frequency timing details, energy, and the first frequency. Additional information can be requested by including the `freeh` keyword (see below).

C.5   Input File Format

The input file format is similar to that well known by Gaussian users. A series of keywords, one per line and indicated by a '%', is followed by the 'route card' (specific job information). Charge and spin is indicated, then the molecule is shown in Cartesian format. This is followed by optional modifications to the Turbomole Control file. Note the location of blank lines in the example (Section 5.7).

C.5.1 Keywords

Keywords are as follows:

- `%nproc` - number of processors to use for the calculation job.

    - Synonym: `%nprocessors`

- `%arch` - parallelization architecture to use for the job.

    - Synonyms: `%architecture`, `%para_arch`

- `%maxcycles` - number of optimization iterations before failing.

- `%autocontrolmod` - DEFAULT - modify the `control` file to include optimizations to speed up the job.

- `%nocontrolmod` - do not modify `control` file as above.

- `%rt` - specify max expected runtime (for any part of job)in hours. Allows backfilling in gridengine queue to speed up job submission. For example, for a 1 hour opt and 4 hour freq, submit at least a `rt` of 4

- `%cosmo` - use turbomole's COSMO solvation model with the specified solvent or `None` to use the idealized solvent (epsilon = infinity). List of available solvents can be shown by running `turbocontrol -s`

Gaussian args, including `%nosave`, `%rwf=[file]`, `%chk=[file]`, and `%mem=[memory]` are silently ignored.

C.5.2   Route Card Options

Route cards take the form of the following:

   `# [jobtype(s)] [joboption(s)]`

Job types available:

- `opt` - Perform a geometry optimization

- `freq` - Perform a frequency analysis. Specify method via numforce or aoforce. default = numforce

- `sp` - Perform a single point energy calculation.

    – Cannot be combined with Opt or Freq

- `ts` - Perform a transition state search to find 1 imaginary vibration.

    – Cannot be combined with Opt or Freq

- `prep` - Prepare the job but do not submit to queue.

    – Cannot be combined with Opt or Freq

Job options available:

- `ri` - Use Turbomole's ri approximation

- `marij` - Use Turbomole's marij approximation

    – Requires `ri`

- `disp` - Use Turbomole's implementation of Grimme's dispersion, version 3

- `aoforce` - Use aoforce for frequency jobs

- `numforce` - Use numforce for frequency jobs

- `freeh` - Use Turbomole's `freeh` thermodynamics data script to extract thermodynamic information after frequency analysis

C.5.3   Title

Following the Route cards, a blank line is added, then a line containing the title of the calculation. This can include any characters, spaces, etc., remaining on only one line. This is followed by a blank line.

C.5.4   Charge and Spin

Charge and spin are listed as two numbers separated by a space: charge spin (eg:0 1)

C.5.5   Geometry

Geometry in xyz coordinate format: Element xcoord ycoord zcoord. Z-matrix geometry is not supported by TurboControl or TurboGo.

C.5.6   Additional control File Modifications

Additional lines to be added or removed from control. Lines automatically added are, as required,:

```
$ricore 0
$paroptions ga_memperproc 900000000000000 900000000000
$parallel_parameters  maxtask=10000
$ricore_slave 1
$maxcor 2048
```

Additional lines may be added, or lines removed, by placing them after the geometry with a `$` (for addition) or `-$` (for removal).

C.5.7 Example Input File

An example input file for benzene in dmf:

```
%nproc=4
%arch=GA
%maxcycles=250
%rt=6
%cosmo=dmf
# opt freq b3-lyp/def2-TZVP ri marij numforce

Benzene Optimization & Frequency

0 1
C  0.000  1.396  0.000
C  1.209  0.698  0.000
C  1.209 -0.698  0.000
C  0.000 -1.396  0.000
C -1.209 -0.698  0.000
C -1.209  0.698  0.000
H  0.000  2.479  0.000
H  2.147  1.240  0.000
H  2.147 -1.240  0.000
H  0.000 -2.479  0.000
H -2.147 -1.240  0.000
H -2.147  1.240  0.000

$disp
-$paraoptions
```

C.6   Code Details

Coverage percentages of code unittests are listed in Table C.1. Results are low for def_op, screwer_op, cosmo_op, freeh_op, turbocontrol, and turbogo because they contain many lines of interacting with GridEngine or TurboMole. Testing is performed via monitoring the status of the scripts as they run in real conditions.

The code style is graded by PyLint and results are shown in Table C.2. PyLint describes coding style, adherence to guidelines, and readability. It does not describe code efficiency or usefulness.

Table C.1 Test Coverage of scripts in Turbocontrol

Name	Statements	Missing	Excluded	Coverage
cosmo_op	106	70	1	34%
cosmo_op_test	17	1	0	94%
def_op	302	226	1	25%
def_op_test	20	1	0	95%
freeh_op	162	55	1	66%
freeh_op_test	27	1	0	96%
screwer_op	71	25	1	65%
screwer_op_test	11	1	0	91%
test_all	18	0	0	100%
turbocontrol	537	319	0	41%
turbocontrol_test	245	24	0	90%
turbogo	343	132	0	62%
turbogo_helpers	383	52	0	86%
turbogo_helpers_test	274	2	0	99%
turbogo_test	98	1	0	99%
	2614	910	4	65%

Table C.2 PyLint Scores for Turbocontrol Code

File	Score /10
test_all.py	2.22
turbogo.py	8.80
turbogo_test.py	6.97
turbocontrol.py	8.55
turbocontrol_test.py	7.18
turbogo_helpers.py	8.81
turbogo_helpers_test.py	7.45
def_op.py	8.18
def_op_test.py	5.71
screwer_op.py	7.36
screwer_op_test.py	6.67
freeh_op.py	8.71
freeh_op_test.py	6.79
cosmo_op.py	8.22
cosmo_op_test.py	6.67

C.7   Citing TurboControl

TurboControl, Turbogo, or any other parts of this code may be cited as: Bulsink, Philip. TurboControl, v. 1.1.0. http://github.org/pbulsink/turbocontrol (accessed June 2014) Change the version number to match the version that you used, and change the accessed date to when you installed or downloaded TurboControl.

check formatting

C.8   License

All third party software is a registered trademark of their respective creators. Use of third party software via this software is limited by the conditions as laid out by the respective companies. License to use this software in no way acts as a license to use any other separate referenced software.

The MIT License (MIT)

Copyright © 2014 Philip Bulsink

Permission is hereby granted, free of charge, to any person obtaining a copy of this software and associated documentation files (the "Software"), to deal in the Software without restriction, including without limitation the rights to use, copy, modify, merge, publish, distribute, sublicense, and/or sell copies of the Software, and to permit persons to whom the Software is furnished to do so, subject to the following conditions:

The above copyright notice and this permission notice shall be included in all copies or substantial portions of the Software.

THE SOFTWARE IS PROVIDED "AS IS", WITHOUT WARRANTY OF ANY KIND, EXPRESS OR IMPLIED, INCLUDING BUT NOT LIMITED TO THE WARRANTIES OF MERCHANTABILITY, FITNESS FOR A PARTICULAR PURPOSE

AND NONINFRINGEMENT. IN NO EVENT SHALL THE AUTHORS OR COPY-RIGHT HOLDERS BE LIABLE FOR ANY CLAIM, DAMAGES OR OTHER LIABIL-ITY, WHETHER IN AN ACTION OF CONTRACT, TORT OR OTHERWISE, ARIS-ING FROM, OUT OF OR IN CONNECTION WITH THE SOFTWARE OR THE USE OR OTHER DEALINGS IN THE SOFTWARE.

Glossary of Terms

CCDC Cambridge Crystallography Data Centre

DFT Density Functional afd

DMF N,N-dimethylformamide

DMSO Dimethylsulfoxide

FTIR Fourier Transform Infrared

GC Gas Chromatography

GUI Graphical User Interface

HOMO Highest Occupied Molecular Orbital

IRC Intrinsic Reaction Coordinate

LUMO Lowest Unoccupied Molecular Orbital

MLCT Metal-Ligand Charge Transfer

MO Molecular Orbital

NMR Nuclear Magnetic Resonance

PCM Polarizable Continuum Model

RWGSR Reverse Water-Gas Shift Reaction

TCD Thermal Conductivity Detector

TD-DFT Time Dependant Density Functional Theorem

TEA Triethylamine

TEOA Triethanolamine

TGA Thermogravimetric Analysis

Bibliography

1. Zeise, W. C. *J. Physik und Chemie (Schweigger)* **1831**, *62*, 393–441.

2. Hunt, L. B. *Platinum Metals Review* **1984**, *28*, 76–83.

3. Griess, J. P.; Martius, C. A. *Compt rendus.* **1861**, *53*, 922–925.

4. Birnbaum, K. *Ann. Chem. (Liebig)* **1868**, *145*, 67–77.

5. Small, B. L.; Brookhart, M. *Journal of the American Chemical Society* **1998**, *120*, 7143–7144.

6. Small, B. L.; Brookhart, M.; Bennett, A. M. A. *Journal of the American Chemical Society* **1998**, *120*, 4049–4050.

7. J. P. Britovsek, G.; C. Gibson, V.; J. McTavish, S.; A. Solan, G.; J. P. White, A.; J. Williams, D.; J. P. Britovsek, G.; S. Kimberley, B.; J. Maddox, P. *Chem. Commun.* **1998**, 849–850.

8. Britovsek, G. J. P.; Bruce, M.; Gibson, V. C.; Kimberley, B. S.; Maddox, P. J.; Mastroianni, S.; McTavish, S. J.; Redshaw, C.; Solan, G. A.; Strömberg, S.; White, A. J. P.; Williams, D. J. *Journal of the American Chemical Society* **1999**, *121*, 8728–8740.

9. Gibson, V. C.; Redshaw, C.; Solan, G. A. *Chemical Reviews* **2007**, *107*, PMID: 17488059, 1745–1776.

10. Boudier, A.; Breuil, P.-A. R.; Magna, L.; Olivier-Bourbigou, H.; Braunstein, P. *Chem. Commun.* **2014**, *50*, 1398–1407.

11. Dudle, B.; Rajesh, K.; Blacque, O.; Berke, H. *Journal of the American Chemical Society* **2011**, *133*, 8168–8178.

12. Jain, K. R.; Herrmann, W. A.; Kühn, F. E. *Coordination Chemistry Reviews* **2008**, *252*, Chiral Catalysis, 556–568.

13. Kuninobu, Y.; Takai, K. *Chemical Reviews* **2011**, *111*, 1938–1953.

14. Kusama, H; Narasaka, K *Bulletin of the Chemical Society of Japan* **1995**, *68*, 2379–2383.

15. Nishiyama, Y.; Kakushou, F.; Sonoda, N. *Bulletin of the Chemical Society of Japan* **2000**, *73*, 2779–2782.

16. Bolm, C.; Kesselgruber, M.; Hermanns, N.; Hildebrand, J. P.; Raabe, G. *Angewandte Chemie International Edition* **2001**, *40*, 1488–1490.

17. Zhao, W.-G.; Hua, R. *Tetrahedron* **2007**, *63*, 11803 –11808.

18. Kawata, A.; Kuninobu, Y.; Takai, K. *Chemistry Letters* **2009**, *38*, 836–837.

19. Hori, H.; Koike, K.; Takeuchi, K.; Ishitani, O. *Chemistry Letters* **2000**, *29*, 376–377.

20. Hua, R.; Tian, X. *The Journal of Organic Chemistry* **2004**, *69*, PMID: 15307759, 5782–5784.

21. Adams, R. D.; Falloon, S. B. *Journal of the American Chemical Society* **1994**, *116*, 10540–10547.

22. Adams, R. D.; Huang, M.; Huang, W.; Queisser, J. A. *Journal of the American Chemical Society* **1996**, *118*, 9442–9443.

23. Zhao, W.-G.; Hua, R. *European Journal of Organic Chemistry* **2006**, *2006*, 5495–5498.

24. Müller, T. E.; Grosche, M.; Herdtweck, E.; Pleier, A.-K.; Walter, E.; Yan, Y.-K. *Organometallics* **2000**, *19*, 170–183.

25. Bartholoma, M.; Valliant, J.; Maresca, K. P.; Babich, J.; Zubieta, J. *Chem. Commun.* **2009**, 493–512.

26. Schibli, R.; Schubiger, A. **2002**, *29*, 1529–1542.

27. Coogan, M.; Fernández-Moreira, V.; Kariuki, B.; Pope, S.; Thorp-Greenwood, F. *Angewandte Chemie International Edition* **2009**, *48*, 4965–4968.

28. Giordano, P. J.; Wrighton, M. S. *Journal of the American Chemical Society* **1979**, *101*, 2888–2897.

29. Fredericks, S. M.; Luong, J. C.; Wrighton, M. S. *Journal of the American Chemical Society* **1979**, *101*, 7415–7417.

30. Sacksteder, L.; Zipp, A. P.; Brown, E. A.; Streich, J.; Demas, J. N.; DeGraff, B. A. *Inorganic Chemistry* **1990**, *29*, 4335–4340.

31. Caspar, J. V.; Meyer, T. J. *The Journal of Physical Chemistry* **1983**, *87*, 952–957.

32. Yam, V. W.-W. *Chem. Commun.* **2001**, 789–796.

33. Feliz, M.; Rodriguez-Nieto, F.; Ruiz, G.; Wolcan, E. *Journal of Photochemistry and Photobiology A: Chemistry* **1998**, *117*, 185 –192.

34. Ruiz, G.; Wolcan, E.; Féliz, M. *Journal of Photochemistry and Photobiology A: Chemistry* **1996**, *101*, 119 –125.

35. Lin, R.; Fu, Y.; Brock, C. P.; Guarr, T. F. *Inorganic Chemistry* **1992**, *31*, 4346–4353.

36. Hino, J. K.; Della Ciana, L.; Dressick, W. J.; Sullivan, B. P. *Inorganic Chemistry* **1992**, *31*, 1072–1080.

37. Walters, K. A.; Kim, Y.-J.; Hupp, J. T. *Inorganic Chemistry* **2002**, *41*, 2909–2919.

38. Striplin, D.; Crosby, G. *Coordination Chemistry Reviews* **2001**, *211*, 163 –175.

39. Martin, T. A.; Ellul, C. E.; Mahon, M. F.; Warren, M. E.; Allan, D.; Whittlesey, M. K. *Organometallics* **2011**, *30*, 2200–2211.

40. Abel, E. W.; Wilkinson, G. *J. Chem. Soc.* **1959**, 1501–1505.

41. Kirkham, W. J.; Osborne, A. G.; Nyholm, R. S.; Stiddard, M. H. B. *J. Chem. Soc.* **1965**, 550–553.

42. Zingales, F.; Sartorelli, U.; Trovati, A. *Inorganic Chemistry* **1967**, *6*, 1246–1248.

43. Gamelin, D. R.; George, M. W.; Glyn, P.; Grevels, F.-W.; Johnson, F. P. A.; Klotzbuecher, W.; Morrison, S. L.; Russell, G.; Schaffner, K.; Turner, J. J. *Inorganic Chemistry* **1994**, *33*, 3246–3250.

44. Martí, A. A.; Mezei, G.; Maldonado, L.; Paralitici, G.; Raptis, R. G.; Colón, J. L. *European Journal of Inorganic Chemistry* **2005**, *2005*, 118–124.

45. Morse, D. L.; Wrighton, M. S. *Journal of the American Chemical Society* **1976**, *98*, 3931–3934.

46. Giordano, P. J.; Fredericks, S. M.; Wrighton, M. S.; Morse, D. L. *Journal of the American Chemical Society* **1978**, *100*, 2257–2259.

47. Granifo, J.; Bird, S. J.; Orrell, K. G.; Osborne, A. G.; Šik, V. *Inorganica Chimica Acta* **1999**, *295*, 56 –63.

48. Orrell, K. G.; Osborne, A. G.; Šik, V.; da Silva, M. W.; Hursthouse, M. B.; Hibbs, D. E.; Malik, K. A.; Vassilev, N. G. *Journal of Organometallic Chemistry* **1997**, *538*, 171 –183.

49. Abel, E. W.; Dimitrov, V. S.; Long, N. J.; Orrell, K. G.; Osborne, A. G.; Pain, H. M.; Sik, V.; Hursthouse, M. B.; Mazid, M. A. *J. Chem. Soc., Dalton Trans.* **1993**, 597–603.

50. Gong, X.; Ng, P. K.; Chan, W. K. *Advanced Materials* **1998**, *10*, 1337–1340.

51. Yu, T.; Tsang, D. P.-K.; Au, V. K.-M.; Lam, W. H.; Chan, M.-Y.; Yam, V. W.-W. *Chemistry – A European Journal* **2013**, *19*, 13418–13427.

52. Lo, K. K.-W.; Louie, M.-W.; Zhang, K. Y. *Coordination Chemistry Reviews* **2010**, *254*, 18th International Symposium on the Photochemistry and Photophysics of Coordination Compounds Sapporo, 2009, 2603 –2622.

53. Lin, T.-P.; Chen, C.-Y.; Wen, Y.-S.; Sun, S.-S. *Inorganic Chemistry* **2007**, *46*, 9201–9212.

54. Slone, R. V.; Yoon, D. I.; Calhoun, R. M.; Hupp, J. T. *Journal of the American Chemical Society* **1995**, *117*, 11813–11814.

55. D. Beer, P.; Timoshenko, V.; Maestri, M.; Passaniti, P.; Balzani, V. *Chem. Commun.* **1999**, 1755–1756.

56. Beer, P. D.; Hayes, E. J. *Coordination Chemistry Reviews* **2003**, *240*, 35 Years of Synthetic Anion Receptor Chemistry 1968-2003, 167 –189.

57. Amoroso, A. J.; Arthur, R. J.; Coogan, M. P.; Court, J. B.; Fernandez-Moreira, V.; Hayes, A. J.; Lloyd, D.; Millet, C.; Pope, S. J. A. *New J. Chem.* **2008**, *32*, 1097–1102.

58. Amoroso, A. J.; Coogan, M. P.; Dunne, J. E.; Fernandez-Moreira, V.; Hess, J. B.; Hayes, A. J.; Lloyd, D.; Millet, C.; Pope, S. J. A.; Williams, C. *Chem. Commun.* **2007**, 3066–3068.

59. Hawecker, J.; Lehn, J.-M.; Ziessel, R. *J. Chem. Soc., Chem. Commun.* **1983**, 536–538.

60. Hawecker, J.; Lehn, J.-M.; Ziessel, R. *Helvetica Chimica Acta* **1986**, *69*, 1990–2012.

61. Takeda, H.; Ishitani, O. *Coordination Chemistry Reviews* **2010**, *254*, Inorganic Reaction Mechanisms A Tribute to Ralph Pearson on the occasion of his 90th birthday, 346 –354.

62. Christensen, P.; Hamnett, A.; Muir, A. V. G.; Timney, J. A. *J. Chem. Soc., Dalton Trans.* **1992**, 1455–1463.

63. Sullivan, B. P.; Bolinger, C. M.; Conrad, D.; Vining, W. J.; Meyer, T. J. *J. Chem. Soc., Chem. Commun.* **1985**, 1414–1416.

64. Caulton, K. G. *European Journal of Inorganic Chemistry* **2012**, *2012*, 435–443.

65. Jurca, T.; Chen, W.-C.; Michel, S.; Korobkov, I.; Ong, T.-G.; Richeson, D. S. *Chemistry – A European Journal* **2013**, *19*, 4278–4286.

66. Juris, A.; Campagna, S.; Bidd, I.; Lehn, J. M.; Ziessel, R. *Inorganic Chemistry* **1988**, *27*, 4007–4011.

67. Black, D. R.; Hightower, S. E. *Inorganic Chemistry Communications* **2012**, *24*, 16 –19.

68. Russell, S. K.; Darmon, J. M.; Lobkovsky, E.; Chirik, P. J. *Inorganic Chemistry* **2010**, *49*, PMID: 20143847, 2782–2792.

69. Tondreau, A. M.; Atienza, C. C. H.; Weller, K. J.; Nye, S. A.; Lewis, K. M.; Delis, J. G. P.; Chirik, P. J. *Science* **2012**, *335*, 567–570.

70. Buckingham, D.; Dwyer, F.; Goodwin, H.; Sargeson, A. *Australian Journal of Chemistry* **1964**, *17*, 315–324.

71. Jurca, T. Charting New Territory in Bis(imino)pyridine Coordination Chemistry., PhD Thesis, University of Ottawa, 2012.

72. Frisch, M. J. et al. Gaussian 09 Revision D.01., Gaussian Inc. Wallingford CT 2009.

73. Becke, A. D. *The Journal of Chemical Physics* **1993**, *98*, 5648–5652.

74. Lee, C.; Yang, W.; Parr, R. G. *Phys. Rev. B* **1988**, *37*, 785–789.

75. Hay, P. J.; Wadt, W. R. *The Journal of Chemical Physics* **1985**, *82*, 299–310.

76. Schäfer, A.; Huber, C.; Ahlrichs, R. *The Journal of Chemical Physics* **1994**, *100*, 5829–5835.

77. Tomasi, J.; Mennucci, B.; Cammi, R. *Chemical Reviews* **2005**, *105*, 2999–3094.

78. Scalmani, G.; Frisch, M. J.; Mennucci, B.; Tomasi, J.; Cammi, R.; Barone, V. *The Journal of Chemical Physics* **2006**, *124* 094107, –.

79. Compain, J.-D.; Bourrez, M.; Haukka, M.; Deronzier, A.; Chardon-Noblat, S. *Chem. Commun.* **2014**, *50*, 2539–2542.

80. Allen, F. H. *Acta Crystallographica Section B* **2002**, *58*, 380–388.

81. Grills, D. C.; Matsubara, Y.; Kuwahara, Y.; Golisz, S. R.; Kurtz, D. A.; Mello, B. A. *The Journal of Physical Chemistry Letters* **2014**, *5*, 2033–2038.

82. Johnson, F. P. A.; George, M. W.; Hartl, F.; Turner, J. J. *Organometallics* **1996**, *15*, 3374–3387.

83. Koike, K.; Okoshi, N.; Hori, H.; Takeuchi, K.; Ishitani, O.; Tsubaki, H.; Clark, I. P.; George, M. W.; Johnson, F. P. A.; Turner, J. J. *Journal of the American Chemical Society* **2002**, *124*, 11448–11455.

84. Smieja, J. M.; Benson, E. E.; Kumar, B.; Grice, K. A.; Seu, C. S.; Miller, A. J. M.; Mayer, J. M.; Kubiak, C. P. *Proceedings of the National Academy of Sciences* **2012**, *109*, 15646–15650.

85. Machan, C. W.; Sampson, M. D.; Chabolla, S. A.; Dang, T.; Kubiak, C. P. *Organometallics* **2014**, *Accepted Article*, DOI: `10.1021/om500044a`.

86. Kou, Y.; Nabetani, Y.; Masui, D.; Shimada, T.; Takagi, S.; Tachibana, H.; Inoue, H. *Journal of the American Chemical Society* **2014**, *136*, 6021–6030.

87. Kalyanasundaram, K.; Kiwi, J.; Grätzel, M. *Helvetica Chimica Acta* **1978**, *61*, 2720–2730.

88. TURBOMOLE V6.5, a development of University of Karlsruhe and Forschungszentrum Karlsruhe GmbH., available from www.turbomole-gmbh.com, 2013.

89. Ahlrichs, R.; Bär, M.; Häser, M.; Horn, H.; Kölmel, C. *Chemical Physics Letters* **1989**, *162*, 165 –169.

90. Tao, J.; Perdew, J. P.; Staroverov, V. N.; Scuseria, G. E. *Phys. Rev. Lett.* **2003**, *91*, 146401.

91. Weigend, F.; Ahlrichs, R. *Phys. Chem. Chem. Phys.* **2005**, *7*, 3297–3305.

92. Haase, F.; Ahlrichs, R. *Journal of Computational Chemistry* **1993**, *14*, 907–912.

93. Treutler, O.; Ahlrichs, R. *The Journal of Chemical Physics* **1995**, *102*, 346–354.

94. Eichkorn, K.; Weigend, F.; Treutler, O.; Ahlrichs, R. **1997**, *97*, 119–124.

95. Eichkorn, K; Treutler, O; Öhm, H; Häser, M; Ahlrichs, R *Chemical Physics Letters* **1995**, *242*, 652 –660.

96. Sierka, M.; Hogekamp, A.; Ahlrichs, R. *The Journal of Chemical Physics* **2003**, *118*, 9136–9148.

97. Deglmann, P.; May, K.; Furche, F.; Ahlrichs, R. *Chemical Physics Letters* **2004**, *384*, 103 –107.

98. Weigend, F. *Phys. Chem. Chem. Phys.* **2002**, *4*, 4285–4291.

99. Von Arnim, M.; Ahlrichs, R. *Journal of Computational Chemistry* **1998**, *19*, 1746–1757.

100. Ahlrichs, R. *Phys. Chem. Chem. Phys.* **2004**, *6*, 5119–5121.

101. Grimme, S.; Antony, J.; Ehrlich, S.; Krieg, H. *The Journal of Chemical Physics* **2010**, *132* 154104, –.

102. Deglmann, P.; Furche, F.; Ahlrichs, R. *Chemical Physics Letters* **2002**, *362*, 511 –518.

103. Grimme, S.; Furche, F.; Ahlrichs, R. *Chemical Physics Letters* **2002**, *361*, 321 –328.

104. Klamt, A.; Schuurmann, G. *J. Chem. Soc., Perkin Trans. 2* **1993**, 799–805.

105. Agarwal, J.; Johnson, R. P.; Li, G. *The Journal of Physical Chemistry A* **2011**, *115*, 2877–2881.

106. Agarwal, J.; Sanders, B. C.; Fujita, E.; Schaefer III, H. F.; Harrop, T. C.; Muckerman, J. T. *Chem. Commun.* **2012**, *48*, 6797–6799.

107. Agarwal, J.; Fujita, E.; Schaefer, H. F.; Muckerman, J. T. *Journal of the American Chemical Society* **2012**, *134*, 5180–5186.

108. Morris, A. J.; Meyer, G. J.; Fujita, E. *Accounts of Chemical Research* **2009**, *42*, PMID: 19928829, 1983–1994.

109. Lukehart, C.; Zeile, J. V. *Journal of Organometallic Chemistry* **1977**, *140*, 309 –316.

110. Shaver, R. J.; Rillema, D. P. *Inorganic Chemistry* **1992**, *31*, 4101–4107.

111. Bulsink, P. TurboControl v1.1.0., `http://github.com/pbulsink/turbocontrol`.

112. Skripnikov, L. Chemissian, a computer program to analye and visualize quantum-chemical calculations., www.chemissian.com, 2013.

113. Blessing, R. H. *Acta Crystallographica Section A* **1995**, *51*, 33–38.

114. Sheldrick, G. Cell_Now., Bruker AXS: Madison, WI, 2004.

115. Sheldrick, G. M. *Acta Crystallographica Section A* **2008**, *64*, 112–122.

116. Spurrier, N. Pexpect, version 3.0., 2013.

117. Open Babel Package, version 2.3.1.

118. O'Boyle, N. M.; Banck, M; James, C. A.; Morley, C; Vandermeersch, T; Hutchison, G. R. *J. Cheminf.* **2011**, *3*, 33.

Todo list